FINAL REPORT ~ FHWA-OK-14-08

BLACK ICE DETECTION AND ROAD CLOSURE CONTROL SYSTEM FOR OKLAHOMA

Tieming Liu, Ph.D.
School of Industrial Engineering and Management
Ning Wang, P.E.
Biosystems and Agricultural Engineering
College of Engineering, Architecture and Technology
Hongbo Yu, Ph.D.
Department of Geography
College of Arts and Sciences
Oklahoma State University

Jeffrey Basara, Ph.D.
Oklahoma Climatological Survey

Yang (Eric) Hong, Ph.D.
School of Civil Engineering and Environmental Science
College of Engineering
The University of Oklahoma

Satish Bukkapatnam, Ph.D.
Industrial and Systems Engineering
Dwight Look College of Engineering
Texas A&M University

BLACK ICE DETECTION AND ROAD CLOSURE CONTROL SYSTEM FOR OKLAHOMA

FINAL REPORT ~ FHWA-OK-14-08
ODOT SP&R ITEM NUMBER 2249

Submitted to:
John R. Bowman, P.E.
Director of Capital Programs
Oklahoma Department of Transportation

Submitted by:
Tieming Liu, Ning Wang, Hongbo Yu
Oklahoma State University

Jeffrey Basara, Yang (Eric) Hong
University of Oklahoma

Satish Bukkapatnam
Texas A&M University

Oklahoma Department
of Transportation

October 2014

TECHNICAL REPORT DOCUMENTATION PAGE

1. REPORT NO. **FHWA-OK-14-08**	2. GOVERNMENT ACCESSION NO.	3. RECIPIENT'S CATALOG NO.
4. TITLE AND SUBTITLE **BLACK ICE DETECTION AND ROAD CLOSURE CONTROL SYSTEM FOR OKLAHOMA**		5. REPORT DATE **October 31, 2014**
		6. PERFORMING ORGANIZATION CODE
7. AUTHOR(S) **Tieming Liu, Ning Wang, Hongbo Yu, Jeffrey Basara, Yang (Eric) Hong, Satish Bukkapatnam**		8. PERFORMING ORGANIZATION REPORT
9. PERFORMING ORGANIZATION NAME AND ADDRESS **Oklahoma State University** **School of Industrial Engineering and Management** **322 Engineering North** **Stillwater, OK 74078**		10. WORK UNIT NO.
		11. CONTRACT OR GRANT NO. **ODOT SP&R Item Number 2249**
12. SPONSORING AGENCY NAME AND ADDRESS **Oklahoma Department of Transportation** **Materials and Research Division** **200 N.E. 21st Street, Room 3A7** **Oklahoma City, OK 73105**		13. TYPE OF REPORT AND PERIOD COVERED **Final Report** **10/01/2012 – 09/30/2014**
		14. SPONSORING AGENCY CODE

15. SUPPLEMENTARY NOTES

16 . ABSTRACT

   Black ice is a thin coating of glazed ice on roadways or other transportation surfaces. Black ice has identical appearance with black pavement and wet road, and it often forms during calm weather. It is highly transparent and thus difficult to see. Black ice usually forms at night or early morning, first on bridges and overpasses (due to their elevated nature and being exposed on all sides), then on the roads as temperatures continue to drop.

   In this project, we develop a prototype decision support system (DSS) to predict and detect black ice formation and pin point dangerous road sections. To reduce accidents caused by back ice, a wireless controlled module control would activate ice-warning and lane-closure signals and lights remotely. The DSS will help Oklahoma Department of Transportation (ODOT) and Oklahoma Department of Emergency Management (OEM) make prompt and effective decisions to reduce the number of traffic accidents caused by ice.

17. KEY WORDS **decision support system, emergency management, black ice, geographic information system, road closure, weather prediction.**	18. DISTRIBUTION STATEMENT **No restrictions. This publication is available from the Materials and Research Div., Oklahoma DOT.**		
19. SECURITY CLASSIF. (OF THIS REPORT) **Unclassified**	20. SECURITY CLASSIF. (OF THIS PAGE) **Unclassified**	21. NO. OF PAGES **74**	22. PRICE **N/A**

SI* (MODERN METRIC) CONVERSION FACTORS

APPROXIMATE CONVERSIONS TO SI UNITS				
SYMBOL	**WHEN YOU KNOW**	**MULTIPLY BY**	**TO FIND**	**SYMBOL**
LENGTH				
in	inches	25.4	millimeters	mm
ft	feet	0.305	meters	m
yd	yards	0.914	meters	m
mi	miles	1.61	kilometers	km
AREA				
in^2	square inches	645.2	square millimeters	mm^2
ft^2	square feet	0.093	square meters	m^2
yd^2	square yard	0.836	square meters	m^2
ac	acres	0.405	hectares	ha
mi^2	square miles	2.59	square kilometers	km^2
VOLUME				
fl oz	fluid ounces	29.57	milliliters	mL
gal	gallons	3.785	liters	L
ft^3	cubic feet	0.028	cubic meters	m^3
yd^3	cubic yards	0.765	cubic meters	m^3
NOTE: volumes greater than 1000 L shall be shown in m^3				
MASS				
oz	ounces	28.35	grams	g
lb	pounds	0.454	kilograms	kg
T	short tons (2000 lb)	0.907	megagrams (or "metric ton")	Mg (or "t")
TEMPERATURE (exact degrees)				
°F	Fahrenheit	5 (F-32)/9 or (F-32)/1.8	Celsius	°C
ILLUMINATION				
fc	foot-candles	10.76	lux	lx
fl	foot-Lamberts	3.426	candela/m^2	cd/m^2
FORCE and PRESSURE or STRESS				
lbf	poundforce	4.45	newtons	N
lbf/in^2	poundforce per square inch	6.89	kilopascals	kPa

APPROXIMATE CONVERSIONS FROM SI UNITS				
SYMBOL	**WHEN YOU KNOW**	**MULTIPLY BY**	**TO FIND**	**SYMBOL**
LENGTH				
mm	millimeters	0.039	inches	in
m	meters	3.28	feet	ft
m	meters	1.09	yards	yd
km	kilometers	0.621	miles	mi
AREA				
mm^2	square millimeters	0.0016	square inches	in^2
m^2	square meters	10.764	square feet	ft^2
m^2	square meters	1.195	square yards	yd^2
ha	hectares	2.47	acres	ac
km^2	square kilometers	0.386	square miles	mi^2
VOLUME				
mL	milliliters	0.034	fluid ounces	fl oz
L	liters	0.264	gallons	gal
m^3	cubic meters	35.314	cubic feet	ft^3
m^3	cubic meters	1.307	cubic yards	yd^3
MASS				
g	grams	0.035	ounces	oz
kg	kilograms	2.202	pounds	lb
Mg (or "t")	megagrams (or "metric ton")	1.103	short tons (2000 lb)	T
TEMPERATURE (exact degrees)				
^oC	Celsius	1.8C+32	Fahrenheit	^oF
ILLUMINATION				
lx	lux	0.0929	foot-candles	fc
cd/m^2	candela/m^2	0.2919	foot-Lamberts	fl
FORCE and PRESSURE or STRESS				
N	newtons	0.225	poundforce	lbf
kPa	kilopascals	0.145	poundforce per square inch	lbf/in^2

*SI is the symbol for the International System of Units. Appropriate rounding should be made to comply with Section 4 of ASTM E380.
(Revised March 2003)

Table of Contents

LIST OF TABLES

LIST OF FIGURES

1. Executive Summary

Black ice is a thin coating of glazed ice on roadways or other transportation surfaces. Black ice has identical appearance with black pavement and wet road, and it often forms during calm weather. It is highly transparent and thus difficult to see. Black ice usually forms at night or early morning, first on bridges and overpasses (due to their elevated nature and being exposed on all sides), then on the roads as temperatures continue to drop.

Black ice is especially hazardous and is a factor in many car accidents. Black ice is deadly, causing numerous accidents each year in Oklahoma and many other states in U.S. According to the Department of Transportation, icy pavement causes nearly 200,000 auto crashes annually accounting for over 10% of all weather related crashes in the U.S. An average of 700 fatalities and over 65,000 injures occur annually due to icy pavement.

Unfortunately, the current static road-side warning signs (such as "Ice May Form on Bridge") simply could not draw enough attention from drivers. Before the presence of dangerous level of black ice is reported and authorities respond, a number of ice-caused accidents could have already happened. Flashing signals with a reduce speed limit are much more effective than static signs to draw drivers' attention and reduce traffic accidents. In the proposed black ice detection and warning system, once the sensor system detects ice formation, yellow lights will start to flash to warn drivers of black ice ahead, and red lights could be turned on by authorized officers to close lanes or read sections in case of emergency. The proposed remote-controlled black-ice detection and warning system could greatly reduce the number of accidents caused by black ice and save hundreds of lives each year.

A major obstacle to widely implement the black ice detection and warning system is that current available sensors specific for black ice detection are too expensive. Typically they cost more than $1,000 per unit. So, it is economically impractical to adopt existing ice sensors for black ice detection across Oklahoma. To tackle this challenge, one of the objectives of this project is to develop a functionally competent and economically feasible sensing system for black-ice detection by using regular temperature, humidity, and light sensors, which are much more viable in terms of cost with less than $100 per unit, to replace expensive ice sensors. If successful, those sensors can be widely applied on bridges and overpasses with a low cost to reduce ice-caused accidents in Oklahoma as well as the nation.

In this project, we develop a prototype decision support system (DSS) to predict and detect black ice formation and pin point dangerous road sections. To reduce accidents caused by back ice, a wireless controlled module control would activate ice-warning and lane-closure signals and lights remotely. The DSS will help Oklahoma Department of Transportation (ODOT) and Oklahoma Department of Emergency Management (OEM) make prompt and effective decisions to reduce the number of traffic accidents caused by ice.

2. Development of a Black Ice Prediction Model

2.1 Introduction

The formation mechanisms and correlated diagnostic and prognostic modeling of black ice have been rigorously studied internationally. With the assistance of elaborate roadside observation networks, or Road weather information systems (RWiS), European nations such as the Czech Republic, Sweden, Denmark, and the United Kingdom have developed diagnostic and prognostic road icing models based on both meteorological parameterization and roadside observations. [24][11][14][7] Efforts have been characterized by sophisticated RWiS infrastructure, but limited forecasting capabilities. [29] However, post-event analyses have resulted in successful meteorological parameterizations of formation mechanisms. [29][11][14] These parameterizations have not been used to their fullest capabilities in the past due to limited spatio-temporal availability of efficiently processed forecast data.

As such, the objective of the present study is to utilize previously tested parameterizations of hoar frost, freezing fog, and frozen precipitation in hopes of developing an efficient, comprehensive black ice forecasting model. Through thorough literature review and careful subsequent analysis of the science behind each parameterization, various parameters were accepted, modified, or replaced altogether. The National Digital Forecast Database (NDFD), Oklahoma Mesonet, and ASOS network are utilized to provide diagnostic and prognostic data ingested by the model. Following complete methodological analysis, a risk analysis of black ice is performed for various regions of Oklahoma, following NOAA-defined climatological regions.

2.2 Literature Review

The foundational prerequisite for black ice formation is maintaining a road surface temperature of below freezing. [11] Quantifying this variable is the most challenging prospect for models attempting to parameterize black ice without direct measurement of road surface conditions. To assist with this task, a multitude of models have been developed to diagnose black ice formation risk using both road weather stations and meteorological parameterizations.

Numerous seemingly applicable models have been investigated by the authors, only to having been found to require supplementary road surface data. These models are wholesomely applicable to situations with RWiS infrastructure, but lie beyond the scope and capabilities of the current model. Each model takes its own approach to solving the primary issue of resolving influences of road-surface temperatures on black ice formation. Sophisticated models based on heat conduction and energy balance have been explored by Rayer (1987) and Sass(1992, 1997), but these models are dependent upon vertical

profiles of temperature within the roadway. [21][24][25] Efforts to extrapolate road conditions to ambient locations without road weather stations have been attempted by Bogren et. al. (1992) and Gustavsson and Bogren (1993). [4]

Shao and Lister (1996) developed a numerical model to solve a road-surface energy balance, but required knowledge of the near-surface profile of static stability, limiting its applicability to observation systems with enhanced vertical resolution. [26] Of note, this radiational model is simplified and used in latter portions of hoar frost parameterization for the current model. Crevier and Delage (2001) parameterized road surface temperature using a similar energy balance, but with combined input from the Global Environmental Multiscale numerical weather prediction model and ambient meteorological observation stations. [6] This model is dependent upon knowledge of snow coverage and an initial value of road-surface temperatures – both of which are not available to the current model. Obviously, without availability of high resolution vertical profiles of atmospheric conditions near the surface or RWiS infrastructure, the applicability of these road surface temperature models is negated.

Hewson et al. (1992) and Takle (1990) overcame this issue through development of models dependent mostly upon variables measured by common surface observation stations (e.g. temperature, wind speed, cloud cover, etc.). These models emphasized the effects of radiational cooling on road surface temperatures to accommodate for a lack of reliable road temperature observations. Takle's system incorporated both hoar frost and frozen precipitation icing mechanisms, with model output being derived from surface thermodynamic and kinematic variables input by a forecaster. [29] Hewson et al. combined an intensive literature review with multiple case studies to parameterize hoar frost formation using data output by weather observation stations throughout the United Kingdom. [11] These two studies were the primary sources of hoar frost parameterization for the current model. However, contradictory arguments for various parameters have been presented through the remainder of this paper.

Although the previously discussed studies focus on hoar frost as the primary black ice formation mechanism, frozen precipitation and freezing fog also obviously pose a significant risk for black ice formation. Gustavsson (1995) indirectly supported freezing fog as a prominent icing mechanism. His results suggest deposition resulting from freezing fog was more significant than that resulting from hoar frost, given similar initial road surface conditions. [9] The authors are not aware of any studies parameterizing freezing fog formation, although Tardif et al. (2007) present a sophisticated typological analysis for generic fog formation. This typology was crucial to the development of the current model's freezing fog parameterizations, under the assumption fog formation mechanisms would be similar during sub-freezing temperatures. This is supported by the independence of Rasmussen et al.'s parameterizations from surface temperature.

Eriksson and Lindqvist (2001) emphasized the importance of road surface temperature on magnitude of impacts resulting from frozen precipitation. They state the road surface temperature is the only variable determining ice formation, although the sophisticated road observation system used in the study permits such specific requirements. As with hoar frost and freezing fog, incorporation of previous meteorological conditions conducive to roadway cooling (e.g. previous night radiational cooling and/or a preceding period of temperatures below freezing) may attempt to accommodate for the lack of road surface temperatures. [29][14] Examination of models dependent upon road-surface energy flux supports the idea that, for instances where road surface temperatures are above freezing, duration and intensity of frozen precipitation events are the most important variables in precipitation related icing. Through latent heat effects of melting and net conductive cooling effects of frozen water on surfaces with temperatures greater than freezing, road surface temperatures may fall below freezing through precipitation influences alone. If road surface temperatures are already below freezing, ice will readily form. [6][26][13][28]

2.3 Current Model Methodology

The optimal spatiotemporal availability of meteorological data within Oklahoma was used in concert with the National Digital Forecast Database (NDFD) to develop a diagnostic and prognostic black ice prediction model. The Oklahoma Mesonet offers 120 automated meteorological observation stations that provide high horizontal resolution of relevant meteorological variables. Additionally, the Automated Surface Observing Systems (ASOS) and Automated Weather Observing Systems (AWOS) provide 54 additional stations throughout the state that offer supplementary data in the form of vertical profiles of cloud cover and precipitation categorization. Refer to Table 2.1 for specific variables used by the Mesonet and ASOS stations in the current model. The NDFD is a database of gridded meteorological forecast data, available up to a 5 km resolution throughout the contiguous United States. The combination of the Oklahoma Mesonet, ASOS/AWOS network, and NDFD gridded forecast database allow for wholesome application of previous studies to the development of the diagnostic and prognostic black ice prediction model.

Obs. System	Variable	Temporal Resolution	Data Format
Mesonet	Temperature Relative Humidity Wind Speed	5 minutes	Magnitude Percent Magnitude

	Wind Direction		Magnitude
ASOS/AWOS	Precipitation Fog Presence Cloud Cover	20 minutes	Categorical Truth Fractional

Table 2.1: Variables utilized from the Oklahoma Mesonet and ASOS/AWOS network for diagnostic risk analysis.

Variable	Temporal Resolution	Format
Temperature Dewpoint Relative Humidity Wind Speed Wind Direction Cloud Cover	3 hours	Magnitude Magnitude Percent Magnitude Magnitude Percent
QPE	6 hours	Magnitude
Precip. Prob.	12 hours	Percent

Table 2.2: Variables utilized from the National Digital Forecast Database (NDFD) for prognostic risk analysis.

The NDFD is the sole source of data for the prognostic model. The NDFD is a database of gridded forecasts output by National Weather Service Weather Forecast Offices, and is a combination of Model Output Statistics data and human judgment. The NDFD currently offers data at a maximum grid resolution of 5 km, which is thus the resolution used by the current model. The NDFD XML server is accessed via Simple Object Access protocol on an hourly basis. A query is first sent to the NDFD for latitude and longitude locations of each grid point throughout Oklahoma. The database is then queried a second time to obtain forecast data for each individual grid point. The data for each individual location is parsed and analyzed for icing risk based on the parameters discussed in subsequent sections. Following black ice risk assessment at all grid points, the data is interpolated using a nearest neighbor interpolation method based on Delaunay triangulation. Please refer to H. Glahn and D. Ruth (2003) for further details. (Figure 2.1)

As previously discussed, the spatio-temporal availability throughout Oklahoma permits direct analysis of black ice risk from observational data. To ensure all necessary meteorological variables for diagnostic black ice risk analysis are available at each Mesonet and ASOS site, each Mesonet site is coupled with the closest ASOS station and each ASOS station is coupled with the closest Mesonet station. This couples the optimal temporal resolution of Mesonet observations with supplementary ASOS data not available to Mesonet sites. The specific reasons for this are also discussed in the subsequent parameterization section. Following diagnosis of icing risk at each Mesonet station, the risk data associated with each station location is, similar to the prognostic analysis, interpolated using a nearest neighbor interpolation method based on Delaunay triangulation. Please see McPherson et al. (2007) and Brock et. al. (1995) for more details on the Oklahoma Mesonet, and the ASOS User Guide [1] for further details. (Figure 2.1)
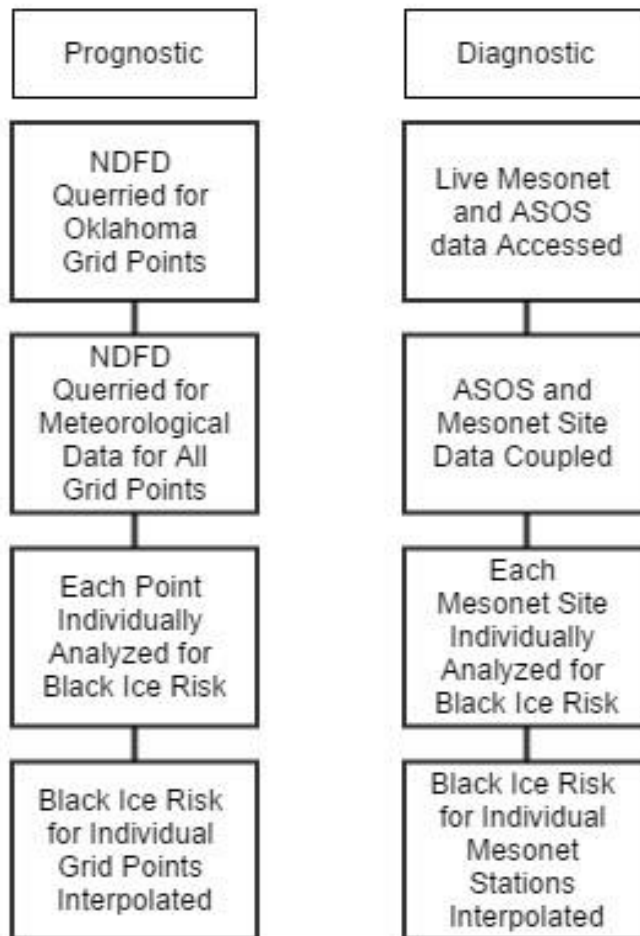
Figure 2.1: Simplified flowchart of procedure for the prognostic and diagnostic risk analyses. Refer to section 3 for further discussion on each.

2.4 Meteorological Parameterization

As previously discussed, Oklahoma current does not have RWiS infrastructure. This makes directly determining road surface temperature impossible, and thus meteorological parameterization is necessary. The main causes of black ice – hoar frost, freezing fog, and frozen precipitation – have all been parameterized accordingly. Frozen precipitation risk parameterization was relegated to the atmospheric surface temperature, risk of precipitation, and previous day meteorological conditions. Hoar frost risk parameterization was entirely de- pendent upon analysis, and subsequent modification of, previously successful parametric studies. Freezing fog risk parameterization was derived from a sophisticated climatological analysis performed on archived Mesonet and ASOS data, guided by the parameters defined in previous fog typological studies such as that of Tardif and Rasmussen (2007). Note, there are slight differences between the diagnostic and prognostic methodologies of the model relating to differences in data availability. For example, ASOS output includes an internalized fog parameterization, rendering the complexity of the current model's fog parameterization unnecessary.

2.4.1 Prognostic Methodology and Parameterization

The NDFD Extensive Markup Language (XML) is queried every hour, accessing forecast data for variables detailed in Table 2.2. Vapor pressure values are calculated using the supplied temperature and dew point data. Each grid point centered within 5-km gridded squares is analyzed for hoar frost, precipitation, and fog related black ice risk at 0, 3, 6, 12, 24, and 48 hours. The prognostic output range was limited to 48 hours to limit the effects of progressively increasing NDFD error with increased forecast range. [8] The data for the entirety of grid points are then interpolated using a nearest neighbor interpolation method based on Delaunay triangulation.

2.4.2 Hoar Frost

Hoar frost occurs when ambient water vapor deposits onto the road surface. This provides arguably the most dangerous aspect of black ice formation due to the inability of the driver to visibly observe the progressive formation of road icing. Furthermore, the complexity of depositional processes leads to complications in the parameterization of hoar frost formation.

A multitude of studies parameterizing hoar frost using meteorological data have been completed and verified using Road Weather information Systems. [11] [14] [7] In turn, this limits the potential negative impacts of being unable to directly verify the current model's hoar frost prediction system. A combination of the work of T. Hewson and N. Gait (1992), E. Takle (1990), M. Karlsson (2001), and J. Shao and P. Lister(2001) was utilized for the development of the current model. Modifications,

discussed and qualified in subsequent portions of this section, have been made to these parameterizations. Refer to Table 2.3 for specific hoar frost parameterizations.

Hoar frost development occurs only when the vapor pressure of the air is greater than the saturation vapor pressure of the roadway surface with respect to ice ($e_{si}(T)e(T)$) directly adjacent to the road surface. [11] There are two instances during which this may occur: 1) instances of prolonged radiational cooling, and 2) advection of warm, moist air over roadways with $T_r < 0°C$. [11][14][9] The hoar frost parameterization is therefore based on the satisfaction of one of these two explicit requirements.

Formation Mechanism	Variable	Parameterization	Risk Index
Radiationally Induced	Time of Day	Sunset < Time < Sunrise	Requirement
	Temperature	$T \leq 2.8\ °C$	Requirement
	Cloud Cover	$\leq 2/8$	0,1
	Wind Speed	$2\ m\ s^{-1} \leq WS \leq 9\ m\ s^{-1}$	0,1
	Previous Night Conditions	$CC \leq 2°C/8\ T \leq 2.8$	0,1
	Ice Crystal Growth Rate	> 0	$0,1 \rightarrow 2$
Advection Induced	Wind Shift	≥ 45	Requirement
	Temperature Increase	> 0	Requirement
	Dewpoint Increase	> 0	Requirement

Table 2.3: Prognostic and diagnostic parameterizations of hoar frost for both radiative and advective hoar frost formation mechanisms.

Due to the inability to directly quantify the road surface temperatures, radiational cooling influences and previous environmental conditions were used to parameterize road surface temperature. The importance of radiational cooling on hoarfrost formation was indirectly supported by Scherm and Bruggen (1995), who found minimal mid-to-upper level clouds to be the most important factor in determining risk of surface condensation, given the absence of low-level clouds. Findings of J. Bogren et al. (2006) also support this. [4] These conditions are also crucial for rapid radiational cooling of the surface. [16]

[18] Furthermore, the influence of previous night environmental conditions on road surface temperature was supported by Hewson and Gait (1992), concluding air temperatures at or below freezing and minimal cloud cover support cooler temperatures. Both of these parameters are directly related to road surface temperatures through surface irradiance and environmental conduction.

Although wind is not conducive to significant near-surface temperature gradients due to production of turbulent mixing and breakdown of the near-surface radiational inversion, downward mixing of moisture to the radiationally cooling surface is dependent upon the presence of near-surface wind generated turbulence. [12] [14] Furthermore, near surface turbulence does not fully mitigate cooling of the roadway surface during periods of ongoing radiational cooling. To prove the continued cooling of the road surface even during instances of near-surface turbulence, a simplified net road-surface thermodynamic energy flux may be analyzed. Net thermodynamic energy flux solely due to turbulent flux and longwave irradiance may be expressed as:

Term	Variable	Units	Order of Magnitude
$\epsilon\sigma T_s^4$	σ T_s	Dimensionless W m^{-2} K^{-4} K	~ 1 ~ 10 $\sim 10^2$
$\rho c_p C_m V\, C_h(T_a - T_s)$ and $\rho C_m V\, C_h(q_a - q_s)$	ρ C_p C_m C_h V $T_a - T_s$ $q_a - q_s$	kg m^{-3} J K^{-1} kg^{-1} Dimensionless Dimensionless m s^{-1} K kg kg^{-1}	~ 1 $\sim 10^3$ $\sim 10^{-3}$ $\sim 10^{-3}$ ~ 1 ~ 1 $\sim 10^{-4}$

Table 2.4: Scales necessary for scale analysis of the road surface energy balance. The first term represents longwave irradiance, while the second and third terms represent the sensible and latent heat fluxes respectively. [32] [35] Refer to section 4.2 for further details.

$$R = -\epsilon\sigma T_s^4 - H - L_\alpha E \tag{2-1}$$

where R is the residual energy, $\epsilon\sigma T_s^4$ is the emitted infrared radiation flux (with being the emissivity coefficient, σ the Stefan-Boltzmann constant, and T_s the road surface temperature), H is the sensible turbulent heat flux, and $L_\alpha E$ is the flux associated with

phase changes of water precipitating onto the road surface. [6] The turbulent flux terms are expressed as:

$$H = -\rho c_p C_m V\, C_h(T_a - T_s) \qquad\qquad (2\text{-}2)$$

$$E = -\rho C_m V\, C_h(q_a - q_s) \qquad\qquad (2\text{-}3)$$

where ρ is the density of air, c_p is the specific heat of air at constant pressure, V is wind speed at 10 meters, C_m and C_h are the surface momentum and moisture transfer coefficients respectively, T is temperature, and q is specific humidity (Refer to Delage and Girard (1992) for details on C_m and C_d). We may perform a scale analysis on Eqn. 2-1 using the scales provided in Table 2.4.

This results in the magnitude of longwave irradiance being on the order of 1 Wm^{-2}, sensible turbulent heat flux on the order of 10^{-1} Wm^{-2}, and latent heat flux on the order of 10^{-4} Wm^{-2}. Thus, even with ongoing surface turbulent flux, given the bounds of hoar frost wind speed parameterization (2 ms^{-1} ≤ WS ≤ 9 ms^{-1}), longwave irradiance dominates road surface temperature. This leads to R, the residual energy, being negative, signifying a loss of energy and cooling of the road surface.

Turbulent downward flux of moisture from the ambient environment toward the road surface enhances hoar frost production rates. [11] [14] Water vapor from the air layer directly adjacent to the road surface deposits, reducing the water content of this air layer. Turbulence rapidly mixes this relatively drier air with the more moist environmental air, increasing the moisture content of the air adjacent to the road surface (and therefore the saturation ratio with respect to ice), enhancing the rate of ice deposition.

Numerous studies have suggested high dew points (e.g. ≥ -1 degrees Celsius in the model of Hewson and Gait (1992)) to be crucial for rapid hoar frost formation. This concept is slightly misunderstood. Environments characterized by higher dew point values – and thus higher vapor pressure – are able to achieve larger values of supersaturation over the roadway given similar road surface temperature. However, the maximum growth rate of an ice crystal occurs well below freezing, and is, in fact, maximized at approximately -15 C. [27] [23] Ice crystal growth rate may be approximated by:

$$\frac{\mathrm{dM}}{\mathrm{dt}} = \rho_i 2\pi D (S_i - 1) G_i(T, P) \qquad\qquad (2\text{-}4)$$

where

$$G_i(T, P) = \frac{1}{\frac{\rho_i L_s^2}{R_v K T_a^2} + \frac{\rho_i R_v T_a}{e_{si}\psi}} \qquad\qquad (2\text{-}5)$$

and

$$\psi = 2.11\text{x}10^{-5}\left(\frac{T}{T_0}\right)^{1.94}\left(\frac{p}{p_0}\right) \qquad\qquad (2\text{-}6)$$

where ψ is the vapor diffusivity, T_0 = 273.15 K, p_0 is the pressure at sea level, ρ_i is the density of ice, D is the diameter of the ice crystal, S_i is the saturation ratio (e / e_{si}), L_s is the latent heat of sublimation, R_v is the gas constant of water vapor, , T_a is the temperature of the ambient environment, and e_{si} is the saturation vapor pressure with respect to ice. [27] For a given pressure field, the growth rate, $dM\ dt^{-1}$ is dependent upon both the supersaturation with respect to ice and the temperature of the ambient environment. Thus, simplified parameterizations used by previous studies solely based on supersaturation are not permissible. Figure 2.2(a) provides a visualization of the growth rate to the supersaturation with respect to ice given varied ambient temperature and dew point depression conditions.

To accommodate for this non-linear relationship between ice crystal growth rate and temperature, a non-linear risk enhancement was incorporated into the model. In the current model, the risk associated with the growth rate of an ice crystal are independent of other variables due to the dynamic nature of road surface temperature parameterizations. Therefore, the maximum growth rate related risk correlates to the highest possible growth rate associated with the air temperature alone. As defined in Eqn. 2-5 diffusional growth of ice crystals is dependent upon the temperature of the ambient environment rather and not the temperature of the ice crystal itself. As such, negligence of the road surface temperature parameterizations for the growth-rate parameterization are qualified.

| | (a) | (b) |
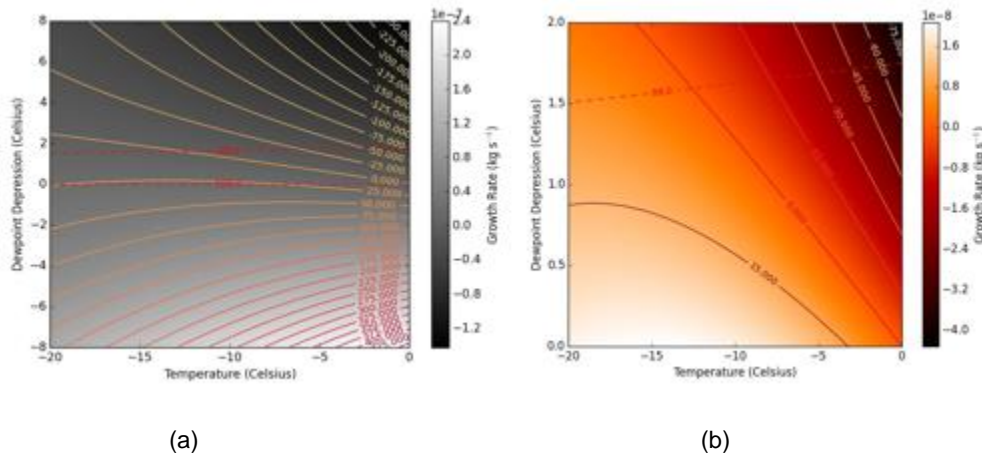
Figure 2.2: Depositional/diffusional growth rate for a range of possible dew point depression and temperature values for: a) hoar frost, and b) freezing fog. Of note, the dashed line in (b) denotes the 88.0 percent relative humidity line. Any region above the line is below 88.0 percent relative humidity and thus is not conducive to fog formation.

Variable	Parameterization	Risk Index
QPE	≥ 0.0 cm	Requirement

Temperature	≤ 0 C	1
Previous Day Previous Night	T ≤ 0 $^\circ$C CC ≤ 2/8 T ≤ 2.8 $^\circ$C	1,0

Table 2.5: Prognostic parameterizations for frozen precipitation.

Of note, Hewson and Gait (1992) and Takle (1990) determined the length of night to be of importance for hoar frost development due to the extended period of time during which radiative cooling occurred. However, the temporal allowances for this parameter were arbitrarily defined using data from a winter characterized by abnormally high near-surface environmental moisture content. These two factors led the authors to removing this parameter from the current model.

2.4.3 Frozen Precipitation

Icing risk associated with frozen precipitation is limited to: 1) the ambient environmental temperature, 2) the probabilistic and quantitative risks of frozen precipitation, and 3) additional parameterization of the road surface temperature through preceding conditions. Refer to Table 2.5 for specific prognostic parameterizations of frozen precipitation.

Variable	Parameterization	Risk Index
Precipitation Type	Frozen	1,0
Temperature	≤ 0 C	1,0
Previous Day Previous Night	T ≤ 0 $^\circ$C CC ≤ 2/8 T ≤ 2.8 $^\circ$C	1,0

Table 2.6: Diagnostic parameterizations for frozen precipitation.

The risk of precipitation leading to icing of road surfaces characterized by above-freezing temperatures is largely dependent upon two variables: 1) The latent heat associated with freezing or melting of water in contact with the road surface 2) The conduction of energy between the frozen precipitation and the roadway.[12][9][4][13] These two variables are not quantifiable through the meteorological parameters provided through the Mesonet and ASOS networks, but can be accounted for through

acknowledgement of precipitation intensity and duration. [4] Unfortunately, the authors are not aware of any existent research interpreting precipitation intensity and duration into risk parameterization. As such, precipitation duration is directly incorporated into the data visualization of the model.

In further attempt to parameterize the likelihood of precipitation related ice formation, preceding environmental conditions were taken into account – as in the hoar frost parameterization. [6] Additionally, freezing temperatures concurrent with frozen precipitation was deemed to lead to enhanced icing risk. Freezing air temperatures lead to progressive cooling of the road surface and enhanced likelihood of liquid water freezing. [4] [15]

2.4.4 Freezing Fog

The fog typology of Rasmussen et al. is used as the foundation for freezing fog parameterization. As defined by Tardif and Rasmussen (2007), the primary fog formation mechanisms are: radiationally induced, evaporative, precipitation enhanced/induced, advection, cloud base lowering. [23] Refer to Table 2.8 for parameterizations of each fog type.

Parameterization of fog dependence on air moisture content is derived from a probability density function of relative humidity data from ASOS and Mesonet archives from the years 2000-2012. All cases of fog were documented and relative humidity values archived. The non-normal distribution was then normalized through a Box-Cox transformation. The BoxCox normalization transformation is defined mathematically as:

$$y = \begin{cases} \frac{x^\lambda - 1}{\lambda} & \lambda \neq 0 \\ \ln(y_i) & \lambda = 0 \end{cases}$$

(2-7)

where λ is varied to ensure the most ideal representation of a normalized distribution. Using the transformed distribution, relative humidity values within two standard deviations

Fog Type	Variable	Parameterization	Risk Index
All	Relative Humidity	≥ 88	Requirement
	Relative Humidity	> 88	.5 → 1
Radiation	Time of Day	Sunset < Time < Sunrise	Requirement
	Wind Speed	≤ 3.2 ms^{-1}	Requirement
	Wind Speed	< 3.2 ms^{-1}	0.5 → 1
	Cloud Cover	≤ 2/8	0,1

	Cooling	dT/dt < 0 C	0,1
Evaporation	Time of Day	Sunrise < Time <= Sunrise + 60 min.	Requirement
	Wind Speed	≤ 3.2 ms^{-1}	Requirement
	Wind Speed	< 3.2 ms^{-1}	.5 → 1
	Cloud Cover	≤ 2/8	0,1
Precipitation	Previous Precipitation	> 0 cm within period of last RH >85%	Requirement
Cloud Base Lowering	Cloud Cover	100 %	Requirement
	Relative Humidity	Increasing from <100% to 100%	Requirement
Advection	Wind Shift	≥ 45	Requirement
	Temperature Increase	> 0	Requirement
	Dewpoint Increase	> 0	Requirement
	Wind Speed	≥ 25 ms^{-1}	Requirement
	Cloud Cover	≥ 75	Requirement

Table 2.7: Prognostic parameterizations for fog formation mechanisms.

Fog Type	Variable	Parameterization	Risk Index
All	ASOS Fog Observation	Yes/No	0,1
	Current Temperature	≤ 0 C	0,1
	Previous Day Previous Night	T ≤ 0 °C CC ≤ 2/8 T ≤ 2.8 °C	1,0

Table 2.8: Diagnostic parameterizations for fog formation mechanisms. of the mean were set as the requirement for fog formation (e.g. ≥ 97.5 percent of events fell within this range, as defined by the Gaussian distribution). The resulting parameterization aligns well with previous research, which commonly establish the minimum relative humidity threshold for fog formation at 90%. [36]

Radiation fog occurs only at nighttime, when net energy flux from the surface is typically less than zero, and only when outgoing longwave radiation dominates surface temperature tendencies. Concurrence of ongoing dominant radiational cooling include the coupling of minimal cloud cover and cooling surface temperatures is suggestive of such radiational cooling. Additionally, low surface wind speeds minimize turbulence, which assists in radiation fog formation. [3] A similar Box-Cox normalization transformation to that used for relative humidity was used in the determination of the maximum wind speed threshold for radiative fog events. The threshold wind speed of 3.3 ms^{-1} is slight higher than established by previous research (range of 2.0 m/s to 3.0 m/s). [30] [3] [36] Of note, the actual risk value assigned to wind speed increases linearly from 0 m s^{-1} to 3.3 m s^{-1}. Although the authors recognize this linear increase in risk is somewhat arbitrary, the authors are not aware of any research discussing the linearity of the relationship between radiative fog and wind speed. Minimal wind speeds have been associated with enhanced radiation fog density, and thus lower wind speeds have been assigned higher risk values. [36] [33]

The formation mechanisms of evaporation related fog closely resemble those of radiatively induced fog. The primary differentiating factor for radiationally induced fog and evaporative fog is the realization of air saturation prior to sunrise. [30] Evaporative fog occurs when the saturation vapor pressure associated with the temperature of the surface of the ground falls to, or below, that of the ambient air, and dew or frost forms on the ground surface. This phenomenon is parameterized through an increase in relative humidity following sunrise, followed by a decrease in relative humidity as boundary layer formation mechanisms begin to dominate the surface layer. Parameterization of radiationally induced surface cooling is also crucial to the development of surface dew, and is thus also included.[19]

Precipitation related fog is only forecastable following precipitation events for the current model. During precipitation events, the primary concern resides with frozen precipitation freezing on the roadway surface, so this is not a significant limiting factor. The enhanced environmental moisture content during precipitation events does not always lead to fog formation, and thus high relative humidity forecasts output by NDFD are not necessarily correlated with precipitation related fog risk for the current model. As such, given enhanced surface moisture following a precipitation event with no further precipitation falling, the risk of precipitation related fog is introduced by the model. [31] [30]

Cloud-base-lowering fog is dependent upon a present low-level cloud deck. Through subsidence coupled with low level moistening and/or cooling, or just simply low level moistening through moisture flux or cooling, a progressive lowering of the cloud deck occurs. [30][3][15] This was parameterized through a present cloud deck with progressive moistening of the surface. Subsidence cannot be parameterized by the current model due to data availability limitations, but the progressive moistening of the surface resulting from the lowering of a cloud base would be captured by NDFD output. This leads to subsidence related boundary layer moistening being indirectly parameterized.

Advection fog is primarily characterized by a significant wind shift associated with a frontal zone and/or thermodynamic boundary. Warm, moist air is advected over a cooler surface, resulting in turbulent mixing of cooler air with warmer air aloft, and eventual saturation. Low level cloud cover is commonly present immediately prior to formation. [9] Low level cloud cover is an indicator of depth of low-level moisture, which is implicative of sustainability of fog. Enhanced turbulence commonly present during advective fog necessitates a deep near-surface layer of moisture to limit entrainment of dry air into the developing fog. As such, low level cloud cover is parameterized as conducive to fog formation during instances of warm, moist advection. [2] [22]

2.4.5 Diagnostic Methodologies

The extraordinary spatio-temporal resolution of meteorological observations across Oklahoma permits the highest resolution black ice formation parameterization diagnostic model to date. The Oklahoma Mesonet provides live meteorological data within five to ten minutes of observation, while ASOS stations provide data every twenty minutes. [17] Furthermore, the spatial resolution of the Oklahoma Mesonet provides an average grid resolution of approximately 40 km, far surpassing resolution of previous attempts based on centralized forecast and observation stations (e.g. Takle (1990) and Rayer(1987)). The spatial resolution of forecasting sites was cited as the primary limiting factor of these studies. Although both the Oklahoma Mesonet and ASOS observation networks provide the necessary variables for ice formation diagnosis, the superior maintenance and quality control measures of the Oklahoma Mesonet support its applicability to the horizontal resolving of the atmosphere. However, the Oklahoma Mesonet does not measure cloud cover and is limited in frozen precipitation measurement capabilities, of which the ASOS observations provide support with precipitation typology and vertical profiles of cloud cover. The Mesonet uses unheated tipping-bucket rain gauges to quantify precipitation, which are inapplicable for live qualitative analysis of frozen precipitation events. [5] Therefore, ASOS precipitation observations are crucial to the ability to analyze potential frozen precipitation related icing events.

To ensure availability of all meteorological variables necessary for black ice risk diagnosis, each Mesonet station is paired with the nearest ASOS station based on simple linear distance. Figure 2.3 provides a visualization for the spatial resolution of the coupling.

Due to the ASOS network's ability to indirectly observe precipitation and fog events (see the ASOS User Guide [1] for details on methodologies), the ASOS network is used as the primary mechanism for diagnosing freezing fog and frozen precipitation events. Should an ASOS station observe ongoing fog, freezing fog, or precipitation, the Mesonet stations paired with that individual ASOS station are checked for temperatures at or below freezing.

If the temperature is at or below freezing, the location of the Mesonet station is flagged for ice occurrence. For precipitation related events, if the ASOS station categorizes the precipitation to be of frozen nature (e.g. snow, sleet, or freezing rain) but the ambient Mesonet stations determine the temperature to be above freezing, then a cautionary risk is displayed at the respective Mesonet locations.

Hoar frost depends primarily upon meteorological variables measured most frequently by Mesonet stations (refer to section 4.2 for discussion). As such, Mesonet locations are utilized as the primary mechanism of hoar frost diagnosis, with ASOS stations providing supplementary cloud cover data. Cloud cover observations for each Mesonet station are derived from the output of each station's respective paired ASOS station.
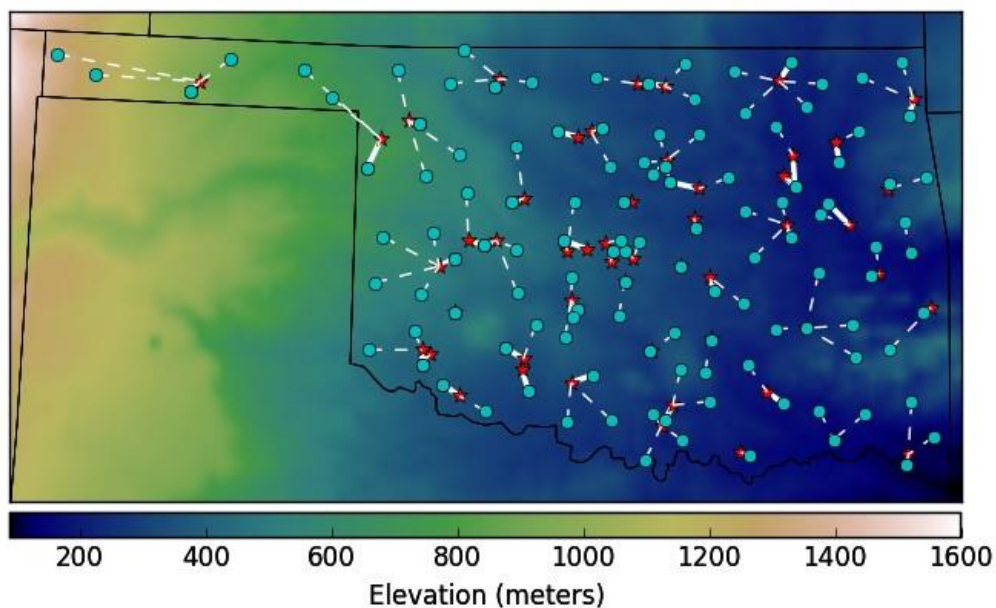

Figure 2.3: A visualization of the coupling of Mesonet sites with ASOS/AWOS stations.

2.5 Summary

Although ice related automobile crashes lead to billions of dollars in financial losses and thousands of lives lost each year, the United States has yet to develop a comprehensive black ice forecasting model. Black ice prediction models based on Road Weather information Systems (RWiS) have been implemented in numerous nations throughout Europe. Through retrospective analysis, multiple studies have developed meteorological parameterizations of black ice formation.

The current study aims to develop a diagnostic and prognostic model to assist in the prevention of black ice related impacts on societal infrastructure. Although the United States does not have as sophisticated of RWiS infrastructure, the elaborate surface meteorological network permits high resolution diagnostic capabilities. Additionally, the National Weather Service offers prognostic data – through the National Digital Forecast Database – with the entirety of variables available necessary for black ice formation forecasting. The developed model synchronizes both sources to provide a comprehensive warning system for the state of Oklahoma. This model offers prognostic data on a 5 kilometer grid - the highest resolution model currently available.

The current model is limited by the lack of road surface observation network throughout the United States. The parameterizations can not be directly verified, and must solely be supported through previous research. Modifications could plausibly be made to the current model should verification mechanisms become available. Additionally, road surface observation stations would supplement provided meteorological parameterizations, and supply a source of road surface temperature initialization. This would both limit necessary parameterizations, and reduce the risk of false alarms.

References

[1] ASOS User Guide. Technical report, National Oceanic and Atmospheric Administration, 1998.

[2] J. Baars, M. Witiw, and A. Al-Habash. Determining Fog Type in the Los Angeles Basin Using Historic Surface Observation Data. In *Proc. 16th Conf. on Probability and Statistics in the Atmospheric Sciences*, 2003.

[3] R. Baker, J. Cramer, and J. Peters. Radiation Fog: UPS Airlines Conceptual Models and Forecast Methods. In *Proc. 10th Conf. On Aviation, Range, Aerospace Meteorology*, 2002.

[4] J. Bogren, T. Gustavsson, and M. Karlsson. Temperature Differences in the Air Layer Close to a Road Surface. *Meteor. Appl.*, 8:385–395, 2006.

[5] F. Brock, K. Crawford, R. Elliott, G. Cuperus, S. Stadler, H. Johnson, and M. Eilts. The Oklahoma Mesonet: A Technical Overview. *J. Atmos. Oceanic Technol.*, 12:5–19, 1995.

[6] L. P. Crevier and Y. Delage. METRo: A New Model for Road-Condition Forecasting in Canada. *J Appl. Meteor.*, 40:2026–2037, 2001.

[7] K. Dejmal and V. Repal. Prediction of Ice Formation on Road Surfaces. *Academic and Applied Research in Military Science*, 8:213–219, 2009.

[8] H. Glahn and D. Ruth. The New Digital Forecast Database of the National Weather Service. *Bull. Amer. Meteor. Soc.*, February 2003.

[9] T. Gustavsson. Analyses of Local Climatological Factors Controlling Risk of Road Slipperiness During Warm-Air Advections. *Int. J. Climatol.*, 11:315–330, 1991.

[10] T. Gustavsson. A Study of Air and Road-Surface Temperature Variations During Clear Windy Nights. *Int. J. Climatol.*, 18:919–932, 1995.

[11] T. Hewson and N. Gait. Hoar Frost Deposition on Roads. *Meteorological Magazine*, 121:1–21, 1992.

[12] E. Hunt, J. Basara, and C. Morgan. Significant Inversions and Rapid In-Situ Cooling at a Well-Sited Oklahoma Mesonet Station. *J. Appl. Meteor. Climatol.*, 46:353–367, 2007.

[13] E. Johnson and D. Esch. Investigation and Analysis of the Paxson Roadway Icing. Technical report, Alaska Department of Highways, 1995.

[14] M. Karlsson. Prediction of Hoar-Frost by use of a Road Weather Information System. *Meteor. Appl.*, 8:95–105, 2001.

[15] D. Koracin, J. Lewis, W. Thompson, C. Dorman, and J. Businger. Transition of Stratus Into Fog Along the California Coast: Observations and Modeling. *J. Atmos. Sci.*, 58:1714–1731, 2001.

[16] R. Lind and K. Katsaros. A model of Longwave Irradiance for Use of Surface Observations. *J. Appl. Meteor.*, 21:1015–1023, 1982.

[17] R. McPherson and Coauthors. Statewide Monitoring of the Mesoscale Environment: A Technical Update on the Oklahoma Mesonet. *J. Atmos. Oceanic Technol.*, 24:301–321, 2007.

[18] P. Mlynczak, G. Smith, A. Wilber, and P. Stackhouse. Annual Cycle of Longwave Radiation. *J. Appl. Meteor. Climatol.*, 50:1212–1224, 2011.

[19] J. Monteith. Dew. *Quarterly Journal of the Royal Meteorological Society*, 83:322–341, 1957.

[20] P. Pisano, L. Goodwin, and M. Rossetti. U.S. Highway Crashes in Adverse Road Conditions. 2008.

[21] P. Rayer. The Meteorological Office Forecast Road Surface Temperature Model. *Meteorological Magazine*, 116:180–191, 1987.

[22] W. Roach. Back to Basics:Fog: Part 3 - The Formation and Dissipation of Sea Fog. *Weather*, 50:80–84, 1995.

[23] R. Rogers and M. Yau. *A Short Course in Cloud Physics*. Butterworth Heineman, 1989.

[24] B. Sass. A Numerical Model for Prediction of Road Temperature and Ice. *J. Appl. Meteor.*, 31:1499–1506, 1992.

[25] B. Sass. A Numerical Forecasting System for the Prediction of Slippery Roads. *J. Appl. Meteor.*, 36:801–817, 1997.

[26] J. Shao and P. Lister. An Automated Nowcasting Model of Road Surface Temperature and State for Winter Road Maintenance. *J Appl. Meteor.*, 35:1352–1361, 1996.

[27] J. Straka. *Cloud and Precipitation Microphysics*. Campbridge University Press, 2009.

[28] L. Symons and A. Perry. Predicting road hazards caused by rain, freezing rain, and wet surfaces and the role of weather radar. *Meteorological Applications*, 4:17–21, 1997.

[29] E. Takle. Bridge and Roadway Frost: Occurrence and Prediction by Use of an Expert System. *J. Appl. Meteor.*, 29:727–735, 1990.

[30] R. Tardif and R. Rasmussen. Event-Based Climatology and Typology of Fog in the New York City Region. *J. Appl. Meteor. Climatol.*, 46:1141–1168, 2007.

[31] R. Tardif and R. Rasmussen. Process-Oriented Analysis of Environmental Conditions Associated with Precipitation Fog Events in the New York City Region. *J. Appl. Meteor. Climatol.*, 47:1681–1703, 2008.

[32] J. Wallace and P. Hobbs. *Atmospheric Science: An Introductory Survey*. Elsevier, 2006.

[33] N. Wescott. Some Aspect of Dense Fog in the Midwestern United States. *Wea. Forecasting*, 22:457–465, 2007.

[34] N. Wood and R. Clark. The Variation of Road-surface Temperatures in Devon, UK During Cold and Occluded Front Passage. *Meteorological Applications*, 6:111–118, 1999.

[35] Q. Zhang, G. Wei, R. Huang, and X. Cao. Bulk transfer coefficients of the atmospheric momentum and sensible heat over desert and Gobi in arid climate region of Northwest China. *Sciences in China Series D: Earth Sciences*, 45:468–480, 2002.

[36] B. Zhou and J. Du. Fog Prediction from a Multimodel Mesoscale Ensemble Prediction System. *Wea. Forecasting*, 25:303–322, 2010.

3. Development of GIS Database and GIS-based Interface for Ice Emergencies

3.1 Introduction

In this task, we acquires various data sets that could be used in supporting road closure decision-making under black ice emergencies. The data collection effort includes both spatial and non-spatial data that could be used in the analysis process.

A geographic information system (GIS) database is then designed and established to efficiently store and manage the acquired data sets. The GIS database is used to support visual and spatial analyses related to road closure decisions in black ice emergencies.

Then a custom GIS interface is developed to support visual and spatial analysis for making road closure decisions under black ice emergencies. A custom toolset with add-in tools is created in ArcGIS to help emergency management officers comprehend the data produced from the black ice prediction module and examine how the predicted black ice event will affect the roads, bridges and local communities. The toolset can help identify roads/bridges that are within the predicted black ice zones and likely to have black ice forming on the surface and shall be closed to prevent potential accidents and life losses.

The custom toolset is developed with ArcObjects in the .NET development environment. ArcObjects is a library of Component Object Model (COM) components which build the basis of ArcGIS. It can be used to customize the ArcGIS Desktop applications, or to build standalone GIS applications. In this project, the add-in tool approach with ArcObjects is chosen to create the custom application tools. An add-in toolbar is developed to support visual and spatial analysis for road closure decisions under black ice emergency scenarios. The toolbar contains four different add-in tools: visual analysis tool, interpolation and animation tool, decision support analysis tool, and sensor feedback tool.

3.2 Acquisition of Data Sets Related to Road Closure Decisions under Black Ice Emergencies

Several key data sources are identified by the research team for data acquisition. These sources include the Bureau of Transportation Statistics (BTS), the U.S. Census Bureau, and the U.S. Geological Survey (USGS).

The following data sets are acquired from the corresponding data sources:

- **Road network**. The road network used in this project is acquired from two major sources. The Bureau of Transportation Statistics (BTS), which is associated with the Research and Innovative Technology Administration (RITA), produces and maintains the National Transportation Atlas Database (NTAD)

(http://www.bts.gov/publications/). The NTAD contains a National Highway Planning Network (NHPN) data set, which is a comprehensive network data set of the nation's major highways, including rural arterials, urban principal arterials and all national highway system routes. The NHPN data set in the 2013 release of NTAD database is acquired and the highways in the state of Oklahoma are extracted to represent the major roads in the state. The U.S. Census Bureau provides a series of TIGER (Topologically Integrated Geographic Encoding and Referencing) products and the TIGER/Line Shapefiles (https://www.census.gov/geo/maps-data/data/tiger-line.html) include a secondary roads layer, which has detailed roads at the street level for each state. The secondary roads data set for Oklahoma from the 2013 TIGER/Line Shapefiles is downloaded and used to show the detailed roads in the state.

- **Bridges**. The NTAD database of BTS also includes a National Bridge Inventory (NBI) data set. The NBI file contains all the bridges located on the major highways with their attribute information, including year built, deck condition ranking, length, the type and name of the road the bridge sits on, etc. The NBI data set from the 2013 NTAD is obtained and used to represent the bridges in Oklahoma.

- **Boundary lines**. The 2013 TIGER/Line Shapefiles also contain boundaries of a certain level of legal entities. As defined by the U.S. Census Bureau (2013), a legal entity is "a geographic entity whose boundaries, name, origin, and area description result from charters, laws, treaties, or other administrative or governmental action". Several boundary line files for Oklahoma, including state, county, census tract, census block group, and census block, are selected and downloaded from the above source.

- **Demographic data**. Population count data at the census block level is collected from the U.S. Census website for the entire Oklahoma (https://www.census.gov/topics/population.html). There are over 270,000 census blocks in Oklahoma. The data set contains the total population count and population count by race for each census block. This data set is used to show the distribution of people in relation to the road network.

- **Elevation data**. The USGS provides the digital elevation model (DEM) data for the entire national. The seamless National Elevation Dataset (NED) covers the United States at a 10-meter resolution national wide (http://ned.usgs.gov/). The DEM data for Oklahoma is obtained and can be used to identify and evaluate the roads and bridges that are prone to forming black ice. A total of 36 tiles of NED raster data covering the territory of Oklahoma were downloaded from the USGS website. The total size of the files is around 20GB. The data is distributed with the North American Datum of 1983 (NAD 1983) and the elevation values are referenced to North American Vertical Datum of 1988 (NAVD1988). The resolution of the data is 1/3 arc-second (approximately 10 meters) in horizontal direction and 1 meter in vertical direction.

3.3 Management of Acquired Data Sets in a GIS Database

As the acquired data sets are from different sources, they are also in different formats and using different spatial referencing systems. In order to efficiently manage the data sets and use them to support visual and spatial analyses in this project, we need to organize the data sets in an integrated database. A GIS database, which can manage both spatial and non-spatial data, presents a logical solution to the data management needs in the project.

In this project, an Esri (Environmental Systems Research Institute) ArcGIS 10.1 geodatabase file is created and used as the GIS database to store and manage all the data sets. The geodatabase file is capable of handling data in different formats, including spatial data in both raster and vector formats, and non-spatial data in tables. The acquired data sets are processed and imported to the created geodatabase. A screenshot of the established ArcGIS geodatabase file for this project is included in Figure 3.1. This figure provides an overview of the GIS database structure and shows how all the data sets are stored and organized in the database.
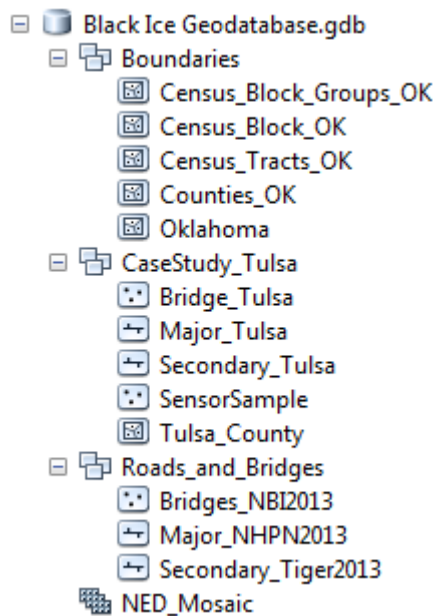

Figure 3.1 The structure of the black ice database

As shown in the figure, the spatial data sets in this project are managed with two types of ArcGIS datasets: *Feature Datasets* and *Raster Mosaic Datasets.* According to Esri's definition, an ArcGIS Feature Dataset is a collection of feature classes as well as other types of vector datasets such as feature-linked annotations, network dataset and topologies, while a Raster Mosaic Dataset is a data model used to organize a collection of raster datasets (e.g., images, digital elevation model data) which will be stored as a catalog and viewed as a whole image (ArcGIS 10.1 Resource Center).

In this project, vector spatial data (e.g., administrative boundaries, roads, bridges) are grouped and organized into several feature datasets distinguished by their theme and

usage in the database. Each feature dataset may contain multiple feature classes and all feature classes in the same feature dataset share the same spatial references, including spatial extend and map projection. Three feature datasets are established in the database.

- The ***Boundaries*** feature dataset contains five feature classes, each of which representing the geographic boundaries of a certain level of legal entities, including the state of Oklahoma, counties, census tracts, census block groups, and census blocks in Oklahoma. These feature classes are created by importing the obtained boundaries files in the TIGER/Line Shapefiles format. Demographic data, including total population count and population count by racial groups, are attached to these feature classes as attributes by joining the boundary file with their corresponding census population data file. Figure 3.2 shows the visual representation of the five feature classes included in this feature dataset.
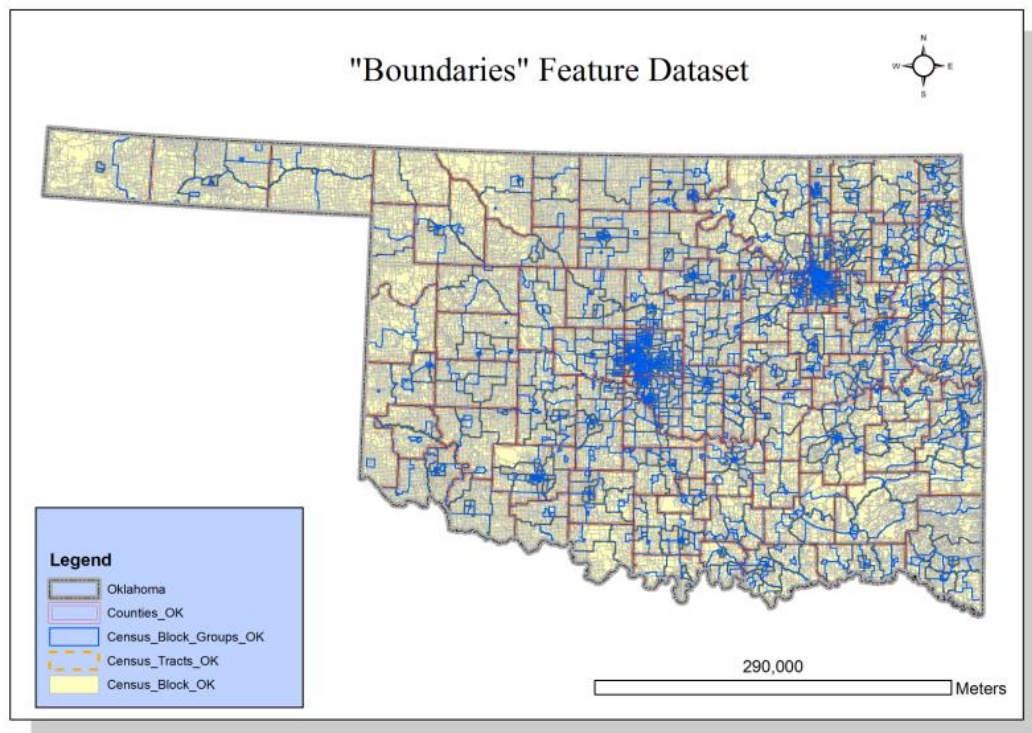

Figure 3.2 "Boundaries" Feature Dataset

- The ***Roads_and_Bridges*** feature dataset is comprised of two linear feature classes representing two road networks in Oklahoma at different levels of details as well as a point feature class representing the central locations of Oklahoma bridges. The "Major_NHPN2013" feature class is derived from the NHPN data set in the 2013 NTAD released by the Bureau of Transportation Statistics. This major road network contains all Oklahoma principle arterials and rural minor arterials. The "Secondary_Tiger2013" feature class is a much more detailed road network, including secondary road, local

neighborhood road, rural road, city street, vehicular trail, ramp, service drive, walkway, stairway, private road for service vehicles, parking lot road, and bike path. As indicated in the name, this feature class is developed from the road layer in the obtained 2013 Tiger/Line Shapefiles database. The "Bridges_NBI2013" feature class is generated by importing the Oklahoma bridge points included in the NBI dataset in the 2013 NTAD database. Figure 3.3 shows the spatial relationship of the three feature classes.
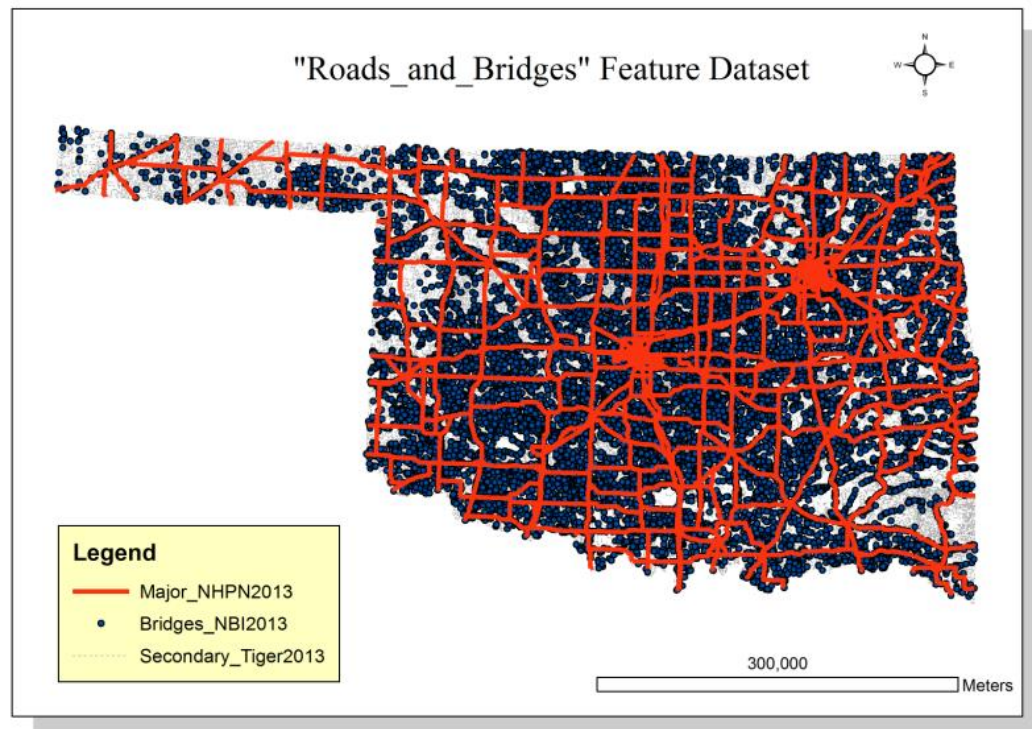
Figure 3.3 "Roads_and_Bridges" Feature Dataset

- The *CaseStudy_Tulsa* feature dataset contains a variety of geographic data in Tulsa County (see Figure 3.4), which is used as a case study area in this project to test-run the decision support system. This dataset contains five feature classes. The "Tulsa_County" feature class is the geographic boundary of Tulsa County, which is a subset of the "Counties_OK" feature class in the "Boundaries" feature dataset. The "Major_Tulsa", "Secondary_Tulsa", and "Bridges _Tulsa" are the subsets of the "Major_NHPN2013", "Secondary_Tiger2013", and "Bridges_NBI2013" in the "Roads_and_Bridges" feature dataset respectively. They are created by clipping the two roads feature classes and the bridge feature class by the geographic boundary of Tulsa County. "SampleSensor" is a point feature class representing the locations of the black ice sensors. As the real sensor location data is not readily available at the moment, a set of hypothetical locations of sensors are generated by randomly selecting 200 points from the Tulsa Bridge feature class.
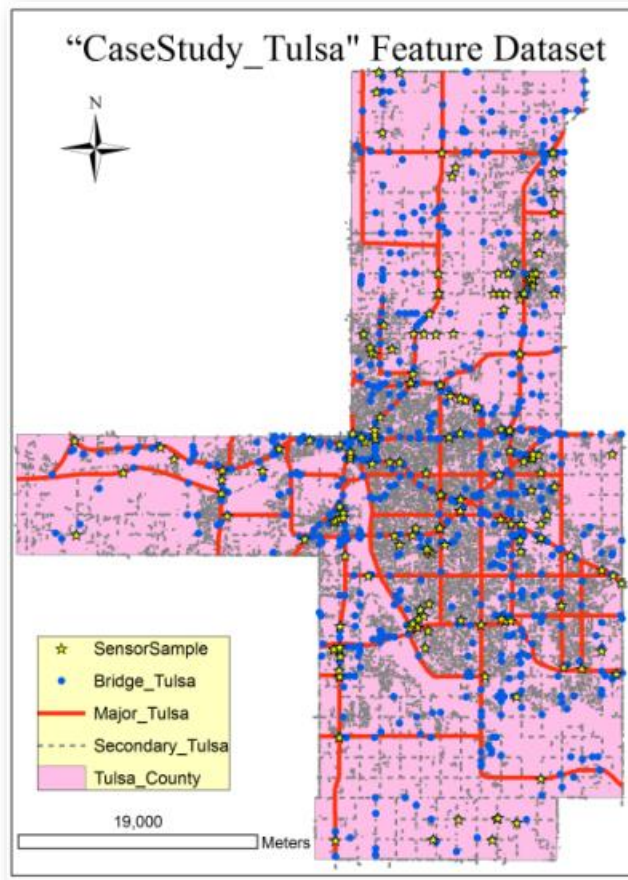
Figure 3.4 "CaseStudy_Tulsa" Feature Dataset

In addition to the feature datasets, a ***NED_Mosaic*** raster mosaic dataset is established to manage raster datasets in the GIS database. The raster mosaic dataset approach allows us to effectively organize the 36 tiles of elevation raster data sets that cover the entire territory of Oklahoma and create an integrated view of the terrain of the state. As shown in Figure 3.5, the raster mosaic dataset provides a seamless terrain representation of Oklahoma at a 1/3 arc-second (about 10-meter) resolution.

3.4 Visual Analysis Add-in Tool

The visual analysis add-in tool implements several methods to help emergency officers comprehend the potential impacts of a black ice event. These methods include interactive viewing of maps composed of different data layers (e.g., Oklahoma terrain layer, different levels of administrative boundaries and road networks) to enhance the understanding of the characteristics and impacts of a black ice event.
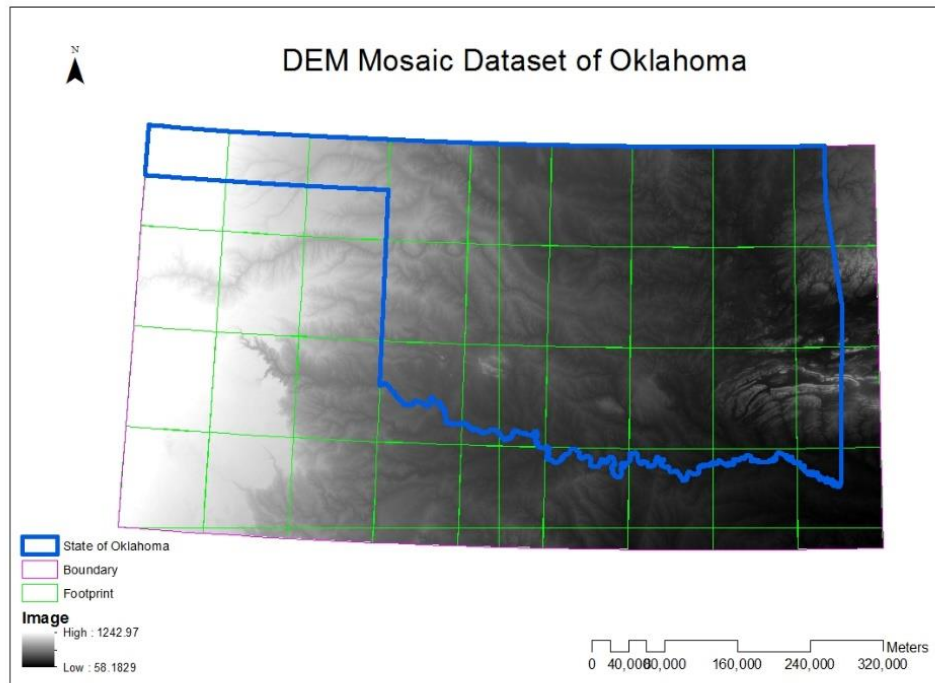
26

Figure 3.5 "NED_Mosaic" Mosaic Dataset

Figure 3.6 is the screenshot of the interface of the visual analysis add-in tool. The tool controls the visibility of nine map layers in the map view. The interface contains three groups of checkboxes. When the checkboxes under the "Administrative Boundaries" group are selected /deselected, the geographic extent of Oklahoma State, Counties, Census Tracts, Census Block Groups and Census Blocks will be shown/hidden in the map window. The checkboxes under "Transportation Networks" group control the visibility of the major/secondary road network and bridges in Oklahoma. When the "National Elevation Data" checkbox is checked, the terrain layer of Oklahoma will be displayed in the map window.

Users can use this interface to control which layer or layer combinations to view on the map and find a set of data layers that can help them better comprehend the impacts of the predicted black ice event.
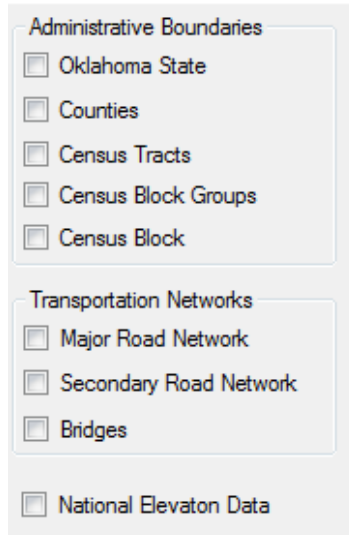
Figure 3.6 Interface of the Black Ice Visual Analysis Add-in Tool

3.5 Interpolation and Animation Add-in Tool

The interpolation and animation tool includes two components. The interpolation tool converts the sequence of black ice prediction files in text format to a sequence of GIS datasets in raster format that can be used to visually demonstrate the spatial distribution of the predicted Black Ice Risk Index (BIRI) values and to overlay with the roads/bridges feature classes to extract the road segments/bridges that are under black ice threats. The animation component is designed for temporal visualization of the development of the black ice event by displaying raster datasets created from the interpolation tool.
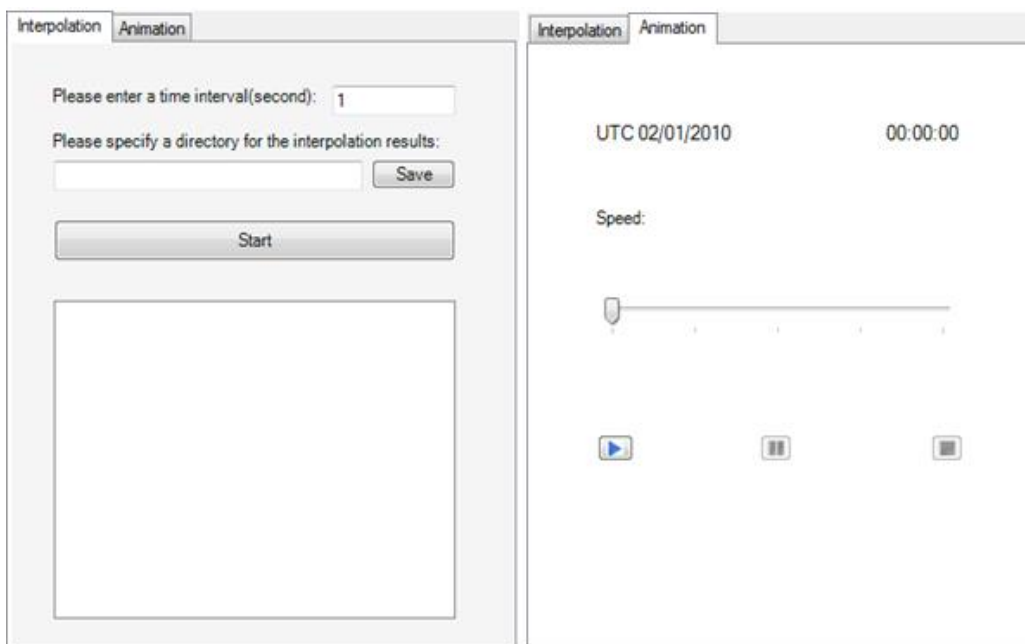

Figure 3.7 Interface of the Black-ice-risk-index Interpolation Add-in Tool

Figure 3.7 shows a screenshot of the interpolation and animation add-in tool interface. The components of this tool can be divided into two function groups: interpolation and animation.

The "interpolation" tab is used to convert the black ice risk index files in .cvs format into GIS files in raster format so that the black ice prediction data can be used to overlay with the roads and bridges dataset for intersect/clip analysis. This interpolation function automatically loads in the predicted BIRI datasets (e.g., a set of black ice live event data comprised of 8 .cvs datasets representing the likelihood of the occurrence of black ice events in Oklahoma at one hour interval from UTC 02/01/2010 00:00:00 AM to UTC02/01/2010 07:00:00AM was used here) at different times, generates point features based on the latitude and longitude information in the BIRI datasets, projects the point features from WGS84 geographic coordinate system to NAD83_Lambert Conformal Conic projected coordinate system and then interpolates the projected point features into raster datasets. The whole process starts when users click on the "Start" button. The system will display a "done" message every time when the process of a specific time layer has been completed. Two parameters can be set by users. The first one is the time interval, which controls how long the next BIRI dataset will be loaded and processed after the previous one is finished. For example, if a user enters 30 in the time interval textbox, the BIRI data of 02/01/2010 01:00:00 AM will not be processed until 30 seconds after the process of the BIRI data of 02/01/2010 00:00:00 AM has completed. The other parameter allows users to set the directory and prefix of the results so the users can easily locate results.

The flow chart in Figure 3.8 illustrates the logical steps used in this add-in tool to convert the .cvs files into point features and interpolate the raster datasets from the point features. According to the flow chart, when users click the "Start" button, it will trigger the process. A BIRI .csv file is loaded into the system. Based on the longitude and latitude information in the .csv file, a make-xy-event operation is applied to the .csv file to create a point feature class. So far the point feature class contains only geographic coordinate system (WGS 1984), for the .csv files do not contain projection information. In order to line up the point feature class with roads/bridges, it is then reprojected to NAD 1983 Contiguous Lambert conformal conic projected coordinate system.

Once the re-projection process is finished, the "create Tin from feature" and "convert Tin to Raster" operations will be applied to convert the points to raster datasets. When carrying out the "convert Tin to Raster" approach, "natural neighbors" conversion method is selected based on the information provided by the OU team. The same process is repeated for all predicted BIRI data at other time instances to create the corresponding BIRI raster datasets.

The "Animation" tab is used to visualize how a black ice event dynamically develops through time. In this function, the output raster datasets of the "interpolation" tab are used to demonstrate the development. When the "start" button is clicked, the animation of the development will be displayed in the map window and the label on top of this tab will update with the corresponding timestamp. When the "Pause" or "Stop" button is clicked, the animation will be temporally paused or terminated.
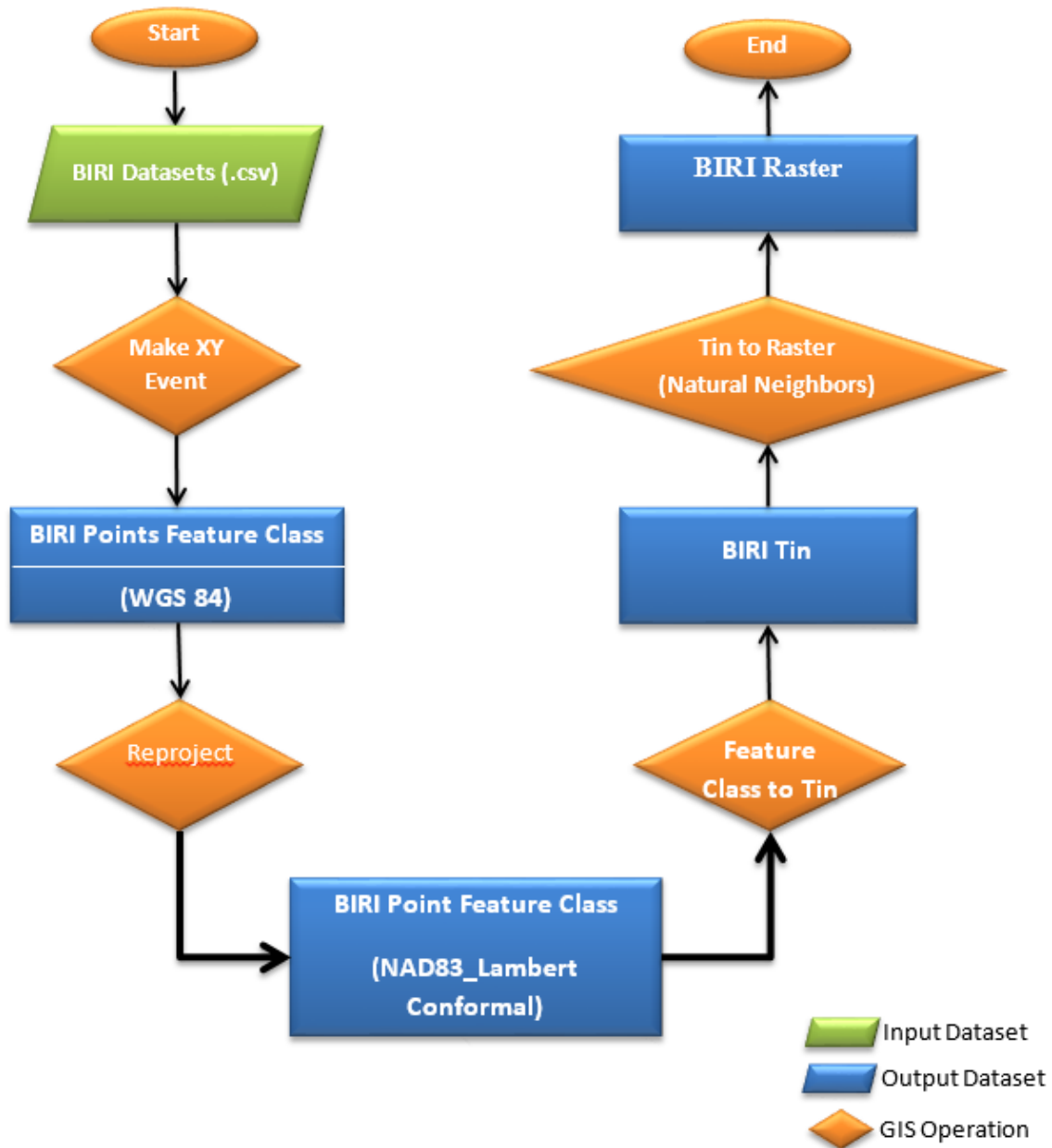

Figure 3.8 Flow Chart of BIRI Interpolation Tool Design

3.6 Decision Support (Spatial Analysis) Add-in Tool

The decision support analysis add-in tool combines the predicted black ice raster dataset (the output of the interpolation tool) and the road networks to identify roads/bridges that will be under potential black ice threats as well as the sample sensors that should be able to detect black ice event.

The tool automatically loads in the predicted black ice raster datasets (the output of the interpolation add-in tool) at different times, delineate the potential black ice warning area, and overlay the area with the road network to identify the road segments and sensors that under threats. Figure 3.9 is a screenshot of the interface of the spatial analysis add-in tool. Similar with the interpolation tool, the whole process of this tool also starts when users click the "Start" button. The system will also display a "done" message every time when the process of a specific time layer has been completed. Three parameters, black ice extent, time interval and the path and prefix of the results, can be set by users. The combobox at the top of the window allows the users to define black ice risk area according to the level of the predicted black ice event. There are four items in the combobox: mild, moderate, serious and extreme which respectively correspond to ">1", ">2", ">3" and ">4"of the black ice risk index.
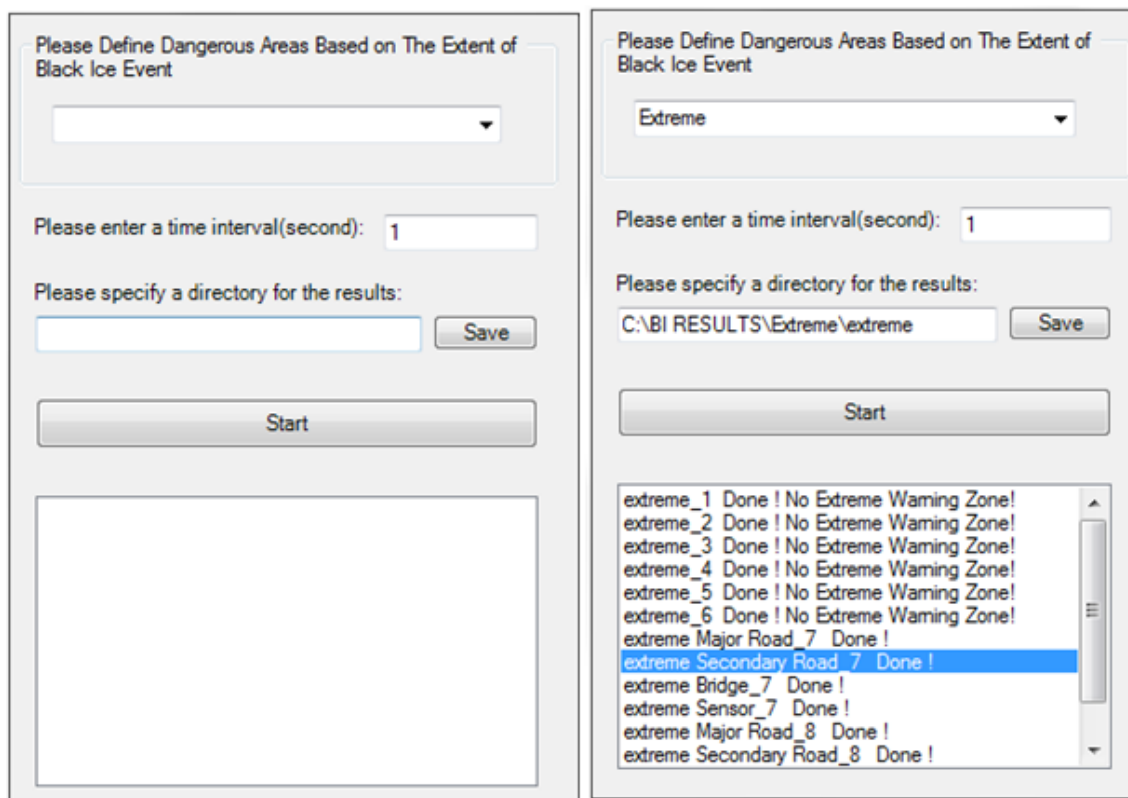

Figure 3.9 Interface of the Spatial Analysis Add-in Tool

The flow chart in Figure 3.10 shows the logical steps used in this add-in tool to extract the potential black ice warning areas and road segments and bridges along with the sensors in the potential black ice warning areas.
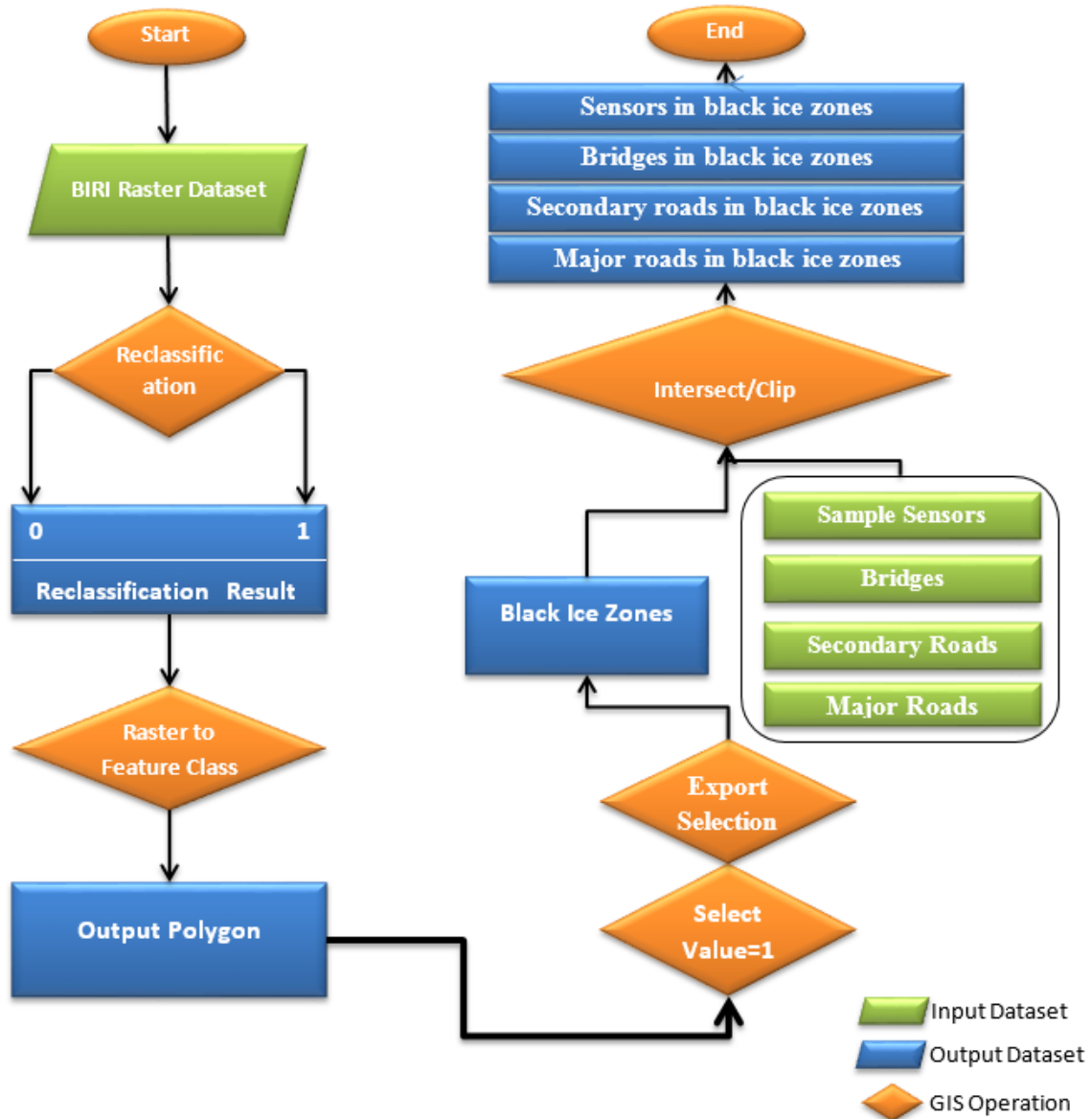

Figure 3.10 Flow Chart of Spatial Analysis Tool Design

According to the flow chart, when users click the "Start" button, it will trigger the process. The BIRI raster dataset (the output of the interpolation add-in tool) is loaded into the system. The values in this raster layer are floats ranging from 0 to 5. Based on a pre-defined threshold value (mild, medium, serious and extreme), reclassification operation is applied to this layer to create a new raster dataset, which only has 1s (if the BIRI value is equal to or larger than the threshold value) and 0s (if the BIRI value is less than the

threshold value). The cells having a value 1 represent the area threatened by the potential black ice event. The reclassified raster dataset is then converted into a feature class through the "Raster to Feature Class" operation. This feature class inherits the value of the reclassified return period dataset and the areas with a value 1 are used to delineate the black ice warning zone. In the next step, two operations are carried out to extract black ice warning zones: "select value = 1" creating a selection of the reclassified feature class containing all polygons whose values equal 1 and "export selection" exporting the selection into a separate feature class. The exported feature class is the black ice zone dataset.

Once the flooding zone dataset is available, the road networks, bridges and the sample sensors feature classes are loaded into the system and intersected (for roads) or clipped (for bridges and sensors) with the black ice zone dataset. This intersect/clip operation generates the final output of the tool, including road segments, bridges and sample sensors that are within the black ice zone. The same process is repeated for all predicted BIRI raster layers at other time instances to create the corresponding road closure suggestion.

3.7 Sensor Feedback Add-in Tool

The sensor feedback add-in tool reads the feedback from the Ice-Detection-Sensor-module, which provides the IDs of on-site sensors that have detected black ice event, and displays the locations of the on-site sensors so that emergency management officers are able to compare the prediction results with the observation results.

The tool automatically loads in the feedback .txt files containing the IDs of Sensors that have detected black ice at different times, select the sample sensors that have identical ID values with the ones in the feedback file, and export the selections as new point feature classes. Figure 3.11 is a screenshot of the interface of the feedback add-in tool. Similar with the interpolation tool, the whole process of this tool also starts when users click the "Start" button. The system will display a "done" message every time when the process of a specific time layer has been completed.
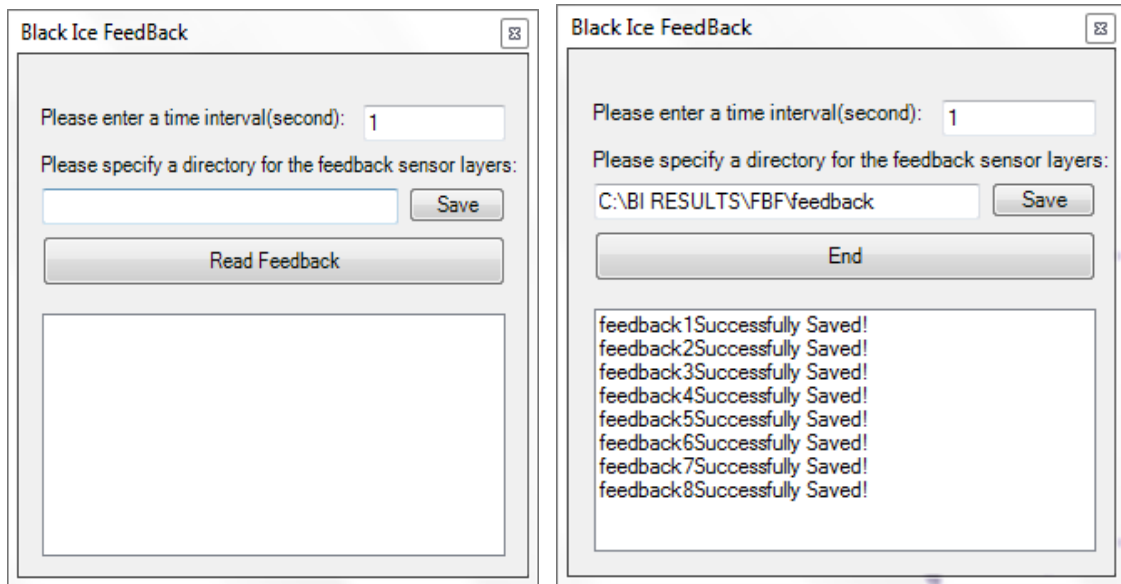
Figure 3.11 Interface of the sensor feedback add-in tool

Reference

[1] U.S. Census Bureau, 2013. Technical Documentation: 2013 Tiger Line/Shapefiles.
http://www.census.gov/geo/maps-data/data/pdfs/tiger/tgrshp2013/TGRSHP2013_TechDoc.pdf

[2] ArcGIS 10.1 Resource Center:
http://resources.arcgis.com/en/help/main/10.1/index.html

4 Development of Conductivity-Based Ice Sensors

4.1 Sensor Selections

The major criteria for selecting black ice sensor include easy-to-uses, rigid, and low-cost. After comparing several ice detection techniques, an electrical conductivity sensors (EC) was selected. Other sensors are either more expensive or not rigid for hash outdoor environment. The EC sensors have been commonly used to measure leaf wetness and frost condition. The sensor output is non-linear with a rapid decrease in resistance relative to an increase in wetness. The sensor costs only around $2 and needs very simple signal conditioning circuit to connect to a datalogger. Figure 4.1 shows the selected sensor and its signal conditioning circuit.
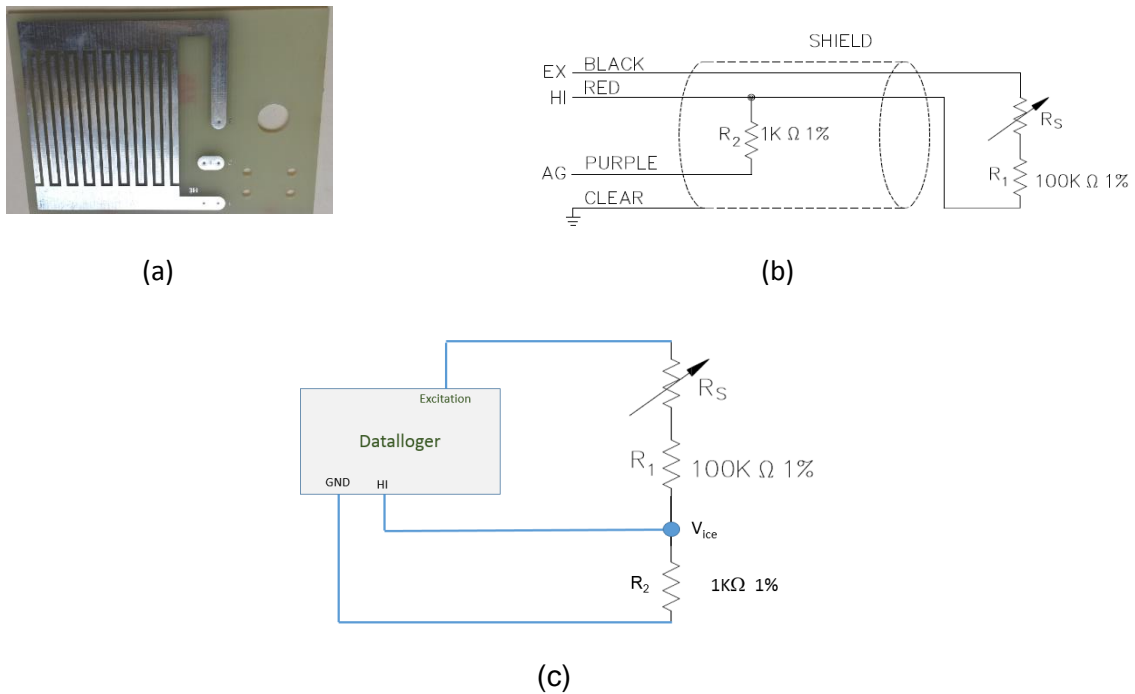

(a) (b)

(c)

Figure 4.1 Selected Black-ice Sensor: (a) electrical-conductivity black-ice sensor; (b) Signal conditioning circuit for the selected sensor (Campbell Scientific, 2010); (c) Wiring diagram for sensor connection with a datalogger

In Figure 1(b) and 1(c), R_s is the resistor varied with the wetness of the sensor surface. When wetness increases, the resistor will decrease. The excitation was set to 5V during the experiment. From the circuit, the sensor output, V_{ice}, can be calculated using Eqn. 4-1:

$$V_{ice} = \frac{R_2}{R_s + R_1} V_{EX} = \frac{1}{100 + Rs} \times 5 = \frac{5}{100 + Rs} \ (V) \qquad (4\text{-}1)$$

Hence, the sensor output voltage will be high when the surface is wet and low when the surface is dry (e.g. possible ice formation). However, it is not possible to confirm ice

formation with only the selected sensor. A thermocouple temperature sensor which, a low-cost sensor, was added to justify the ice formation situation.

4.2 Preliminary Tests on the Selected Black Ice Sensor

To verify the sensor performance, several tests were conducted under lad condition. The test platform included a freezer, a humidifier, three thermocouple sensors, two humidity sensors, two selected sensors, three fans, a Campbell Scientific datalogger, a control box, a concrete sample, and an asphalt sample. The control box had two relays circuit to control the ON/OFF of the freezer and the humidifier, respectively. The freezer would be on until the air temperature insider the freezer was below -10°C. The two humidity sensors were installed on the concrete and the asphalt, respectively. The humidifier would be turned off if the saturation humidity on any one of the humidity sensors was reached. The three thermocouple sensors were used to monitor the temperature changes in the air, on the surface of concrete, and on the surface of asphalt inside the freezer. Three fans were kept on during the test to generate uniform distribution of humidity inside the freezer. Each sensor were mounted on a frame to allow a 45° inclination from the concrete/asphalt surface. This was to avoid any accumulation of water, dust, mud, or other objects on sensor surface to affect the sensor reading. Figure 4.2 shows the test platform. Figure 4.3 shows the components outside of the freezer.

(a)
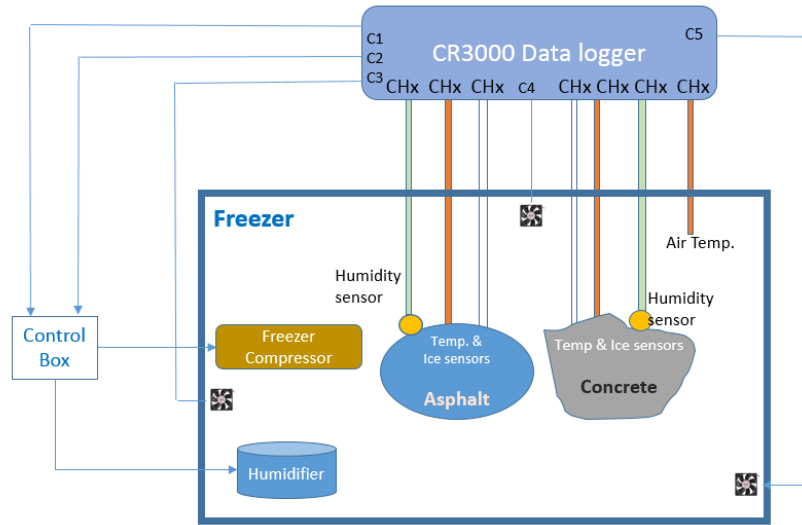
(b)

Figure 4.2 Lab test platform: (a) a photo of test setup (b) a wiring diagram of the test platform

Figure 4.3 Other components of test platform

1. Temperature variation monitoring

Goal: To verify the performance of temperature measurements

Test condition: Freezer was turned on during the test.

Data collection: A data file was collected by the datalogger including three temperatures. The sampling interval was set at every 30 seconds. The humidifier was turned on until the air temperature readings was below zero.

Results: Figure 4.4 shows the results of temperature measurements. The temperature dramatically changed at the beginning of the experiment and gradually decreased with time. The air temperature was well below those on the surface of the concrete/asphalt, but with same trend. Hence, the temperature sensor should be installed close to the surface of the road.
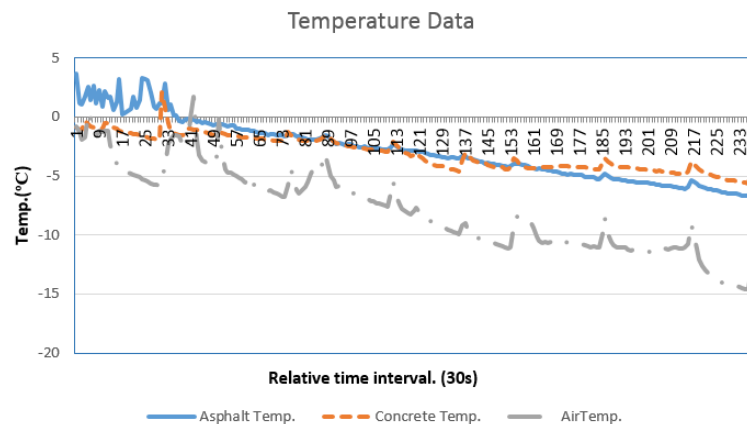

Figure 4.4. Temperature changes during the initial test

2. Ice formation monitoring

Goal: To verify if the selected sensor would react when ice was formed.

Test condition: Freezer was turned on during the test. The humidifier was on until the air temperature reached below 0°C

Data collection: A data file was collected including three temperatures and two ice sensor outputs. The sampling interval was set at every 30 seconds.

Results: Figure 4.5 shows the results of ice sensor tests. During the test, the freezer was opened multiple times to examine if ice was formed on the wetness sensor and the surface of pavement samples. Thus, the temperature changed in a sinusoid pattern throughout the experiment. The ice on the asphalt surface was examined manually and found that after No.136 data point, the surface was icy. The ice was considerable thick at the manual observation and could confirm that the rise of the readings indicated the ice formation. The selected ice sensor provided relative stable readings after ice was formed. However, due to the disturbance of opening the freezer and the saturation of humidity inside the freezer, the 190-210 readings had a big changes.
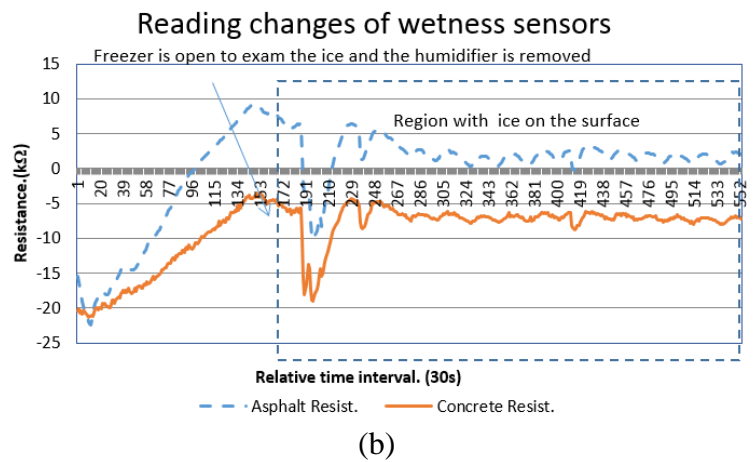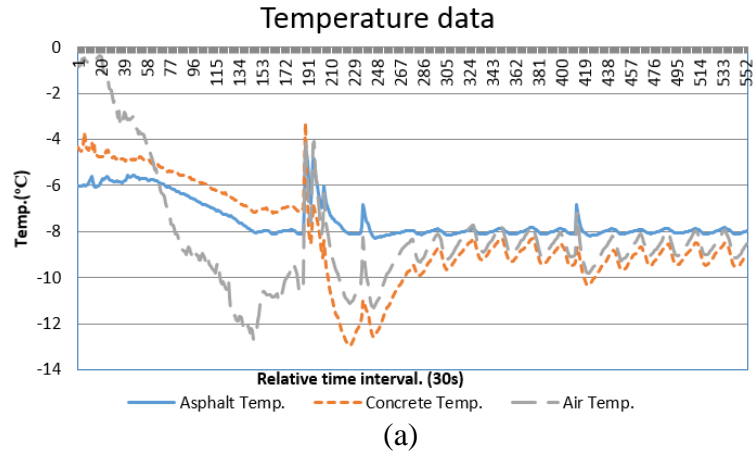
Temperature data

(a)

Reading changes of wetness sensors

(b)

Figure 4.5. Results from the selected sensor tests: (a) Temperature readings; (b) Outputs of selected ice sensors

3. Temperature effect on the selected ice sensor

Goal*:* To verify that the selected sensor output would not change with surrounding temperature changes.

Test conditions*:* The freezer was on during the test. The fans and the humidifier remained off. Two selected ice sensors were placed inside the freezer, one on concrete and another on Asphalt

Results*:* When the freezer was turned on, the inside temperature started decreasing. The results showed that the output of the black sensor had minimum variations with temperature as shown in Figure 4.6.
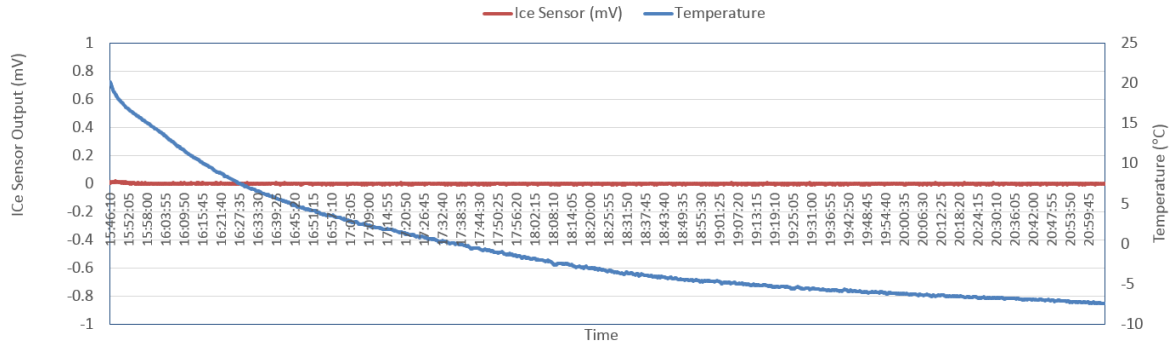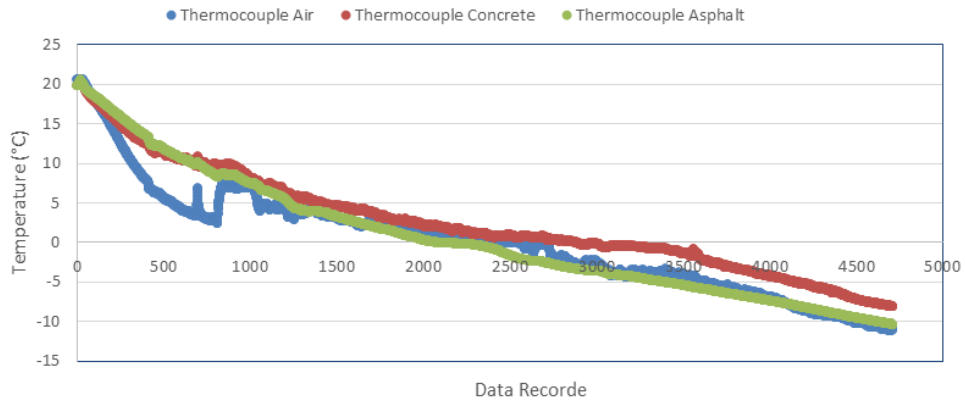
Figure 4.6 Test results on the selected ice sensor output vs. temperature

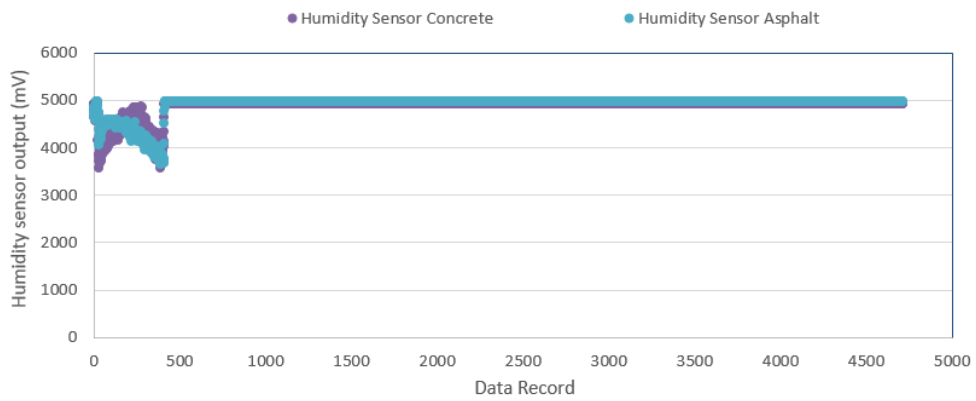4. *Test on black ice formation with temperature, humidity, and selected black ice sensors.*

Goal: To seek an approach to precisely measure the black ice formation with integrated information of temperature, humidity and the output of selected black ice sensor

Test conditions: The freezer, the humidifier, and the three fans were turned on from the beginning of the test. The humidity level were maintained at the saturation.

Results: During the test, the humidity increased from 50% (2500mV) to 98% (4900mV) and stayed at the same level throughout the experiment. As the temperature decreased, wet vapor inside the freezer started to condense. More water drops were formed on the black ice sensor which led to the increase of the sensor readings. When the temperature reached below zero, the black ice sensor output started decrease sharply due to partial ice formation. The more ice formed, the slower the decrease of black ice sensor output. The result also shows that the black ice was formed at different time on asphalt and concrete. This was due to the distances between the humidifier and the sensors respectively and non-uniform distribution of water vapor insider the freezer. Further tests were conducted to verify this observation. At around -4°C, a thin layer of ice was formed on the black sensors. The black ice sensor output reached a steady state (Figure 4.7). Hence, with a collaboration of a temperature sensor and the proposed black ice sensor, the black ice formation could be measured.

(a)

(b)
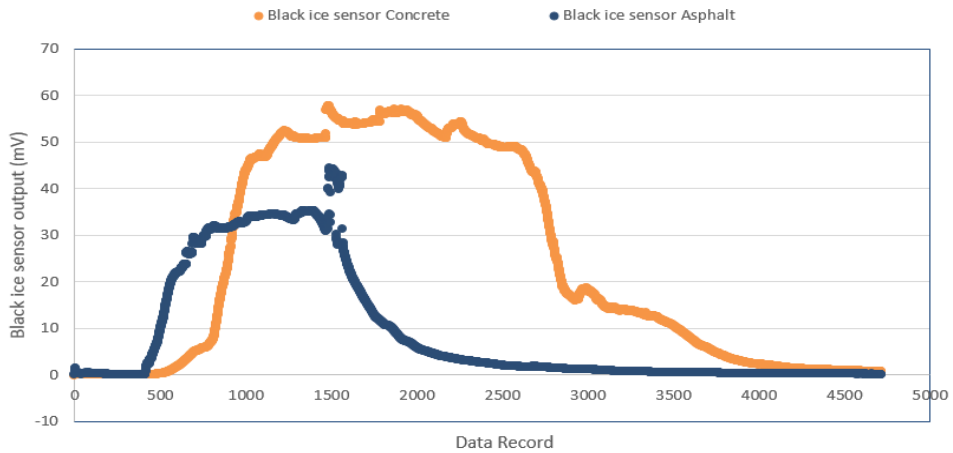
(c)

Figure 4.7 Test results with integrated information of (a) Temperature profile; (b) humidity profile; and (c) the selected black-ice sensor outputs

41

4.3 Performance Tests on the Integrated Black Ice Formation Sensing and Warning System

The integrated black ice formation sensing and warning system was tested under lab condition with the test platform. Two group of tests were conducted with different goals.

Test group 1: Repeated tests were conducted to study the behavior of the two sensors and determine the conditions indicating the ice formation. Figure 4.8 shows an example of the data from test group 1.
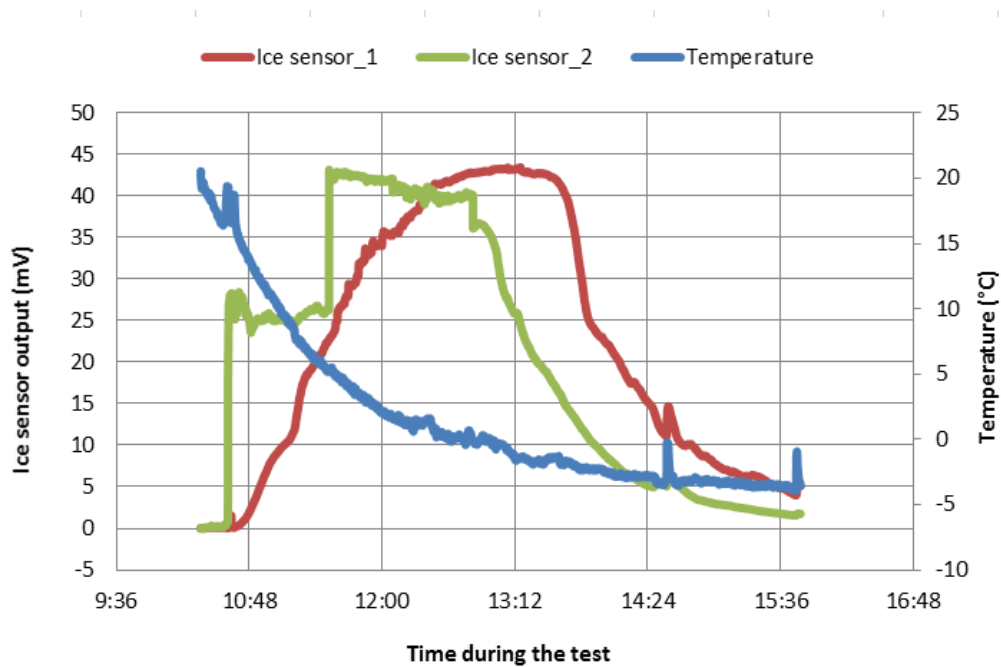

Figure 4.8 An example of the data from test group 1

If humidity was available, the output of the selected sensor would increase. If the temperature kept dropping below 0°C, ice on the surface of the sensor started forming. When the output of the ice sensor dropped from its maximum for about 38mV and the temperature was below -3°C,   ice formation fully on the sensor surface was concluded. Repeated tests were conducted which gave very similar results. Hence, these two conditions were then used to control the warning unit.

Test group 2: Repeated tests were conducted to verify the functions of ice formation sensing and the warning control. Figure 4.9 shows a flow chart of the datalogger control program. The value in the condition to turn on the warning light could be changes through roadside collaboration. Figure 4.10 provides an example of data collected from the developed system. The warning light was on when the ice formation signal was given.
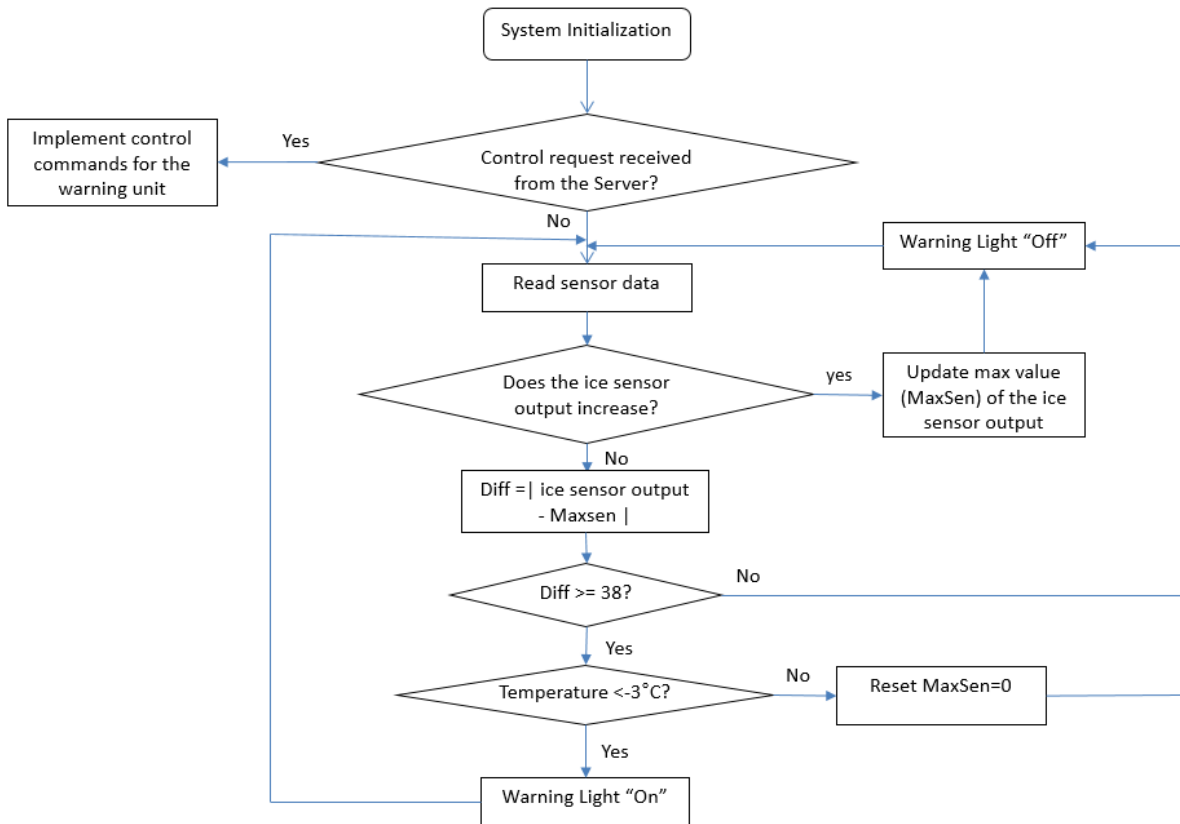
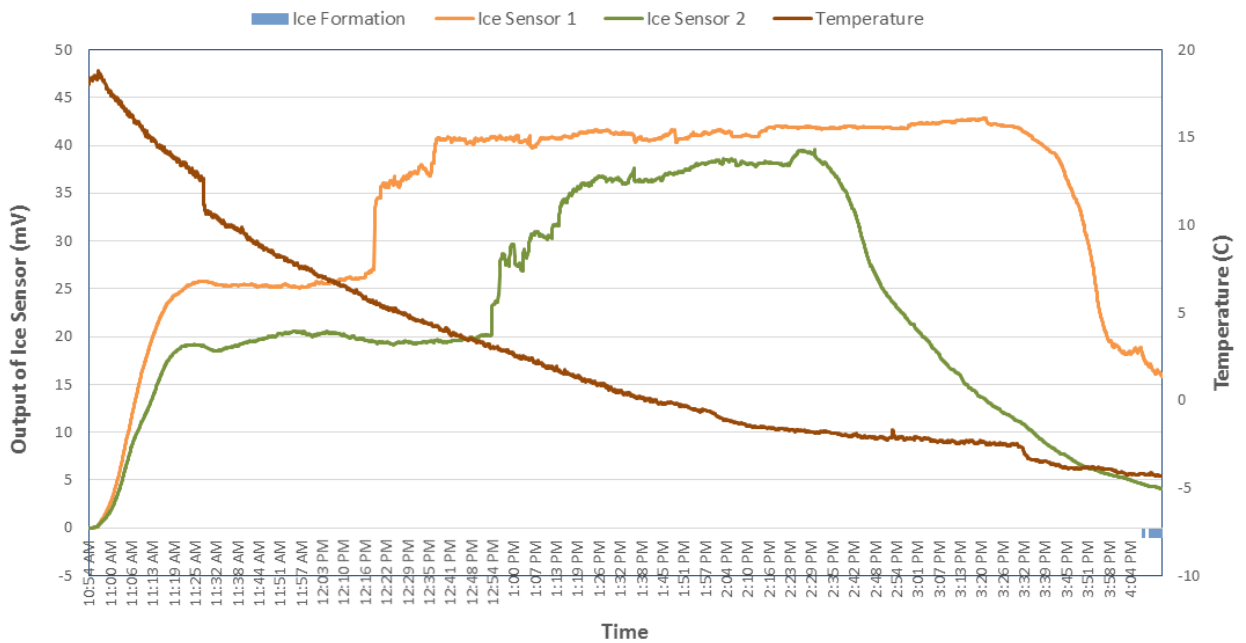Figure 4.9 Flow chart of the datalogger control program

Figure 4.10 An example of the data from test group 2

43

5. Development of Piezoelectric Ice Sensor System

5.1 Background

Piezoelectric materials such as dielectric crystals, ceramic, and plastic materials generate electrical charge by converting the mechanical activity (i.e. a vibration) to an electrical field. Vice versa, they could also generate a mechanical movement when excited by the electrical charges [4]. The heart of the piezoelectricity's ability to generate electricity is from the dipoles formed by the positive and negative ions. In static state, these ion charges are balanced due to the symmetry of the crystal structure. With an excitation from any mechanical movement, the crystal structure is deformed. Because the symmetry is lost, the differences in ion charges cause an electric filed across the crystal [4].

The piezoelectric materials are commonly known to be used in a detection of pressure variations such as a microphone, and ultrasonic transducers, or creating sounds with excitation from electricity such as a buzzer. In the latter application, the transducer could be forced to vibrate at the maximum vibration amplitude by applying an alternating current (AC) at transducer's natural frequency. The resonance frequency, f, can be expressed as a function of a mass, m, and a stiffness, k, as shown in the equation below [5]:

$$f = \frac{1}{2\pi}\sqrt{\frac{k}{m}}$$

According to the equation above, the resonant frequency, f, will be directly correlate with the stiffness, k, of the piezoelectric transducer whereas the mass, m, would be inversely proportional to f. With this assumption, naturally, when placing the piezoelectric transducer in air state, the resonance frequency could be arbitrarily calculated as f_{air}. Next, if we place the same piezoelectric transducer in water, the effective stiffness of the piezoelectric transducer due to the adhesion between water and its surface will be negligible [6]. The resonance frequency in this case would be affected by the effective mass of the piezoelectric transducer and water. Thus, the new resonance frequency, f_{water}, should decrease ($f_{air} < f_{water}$). Next, in the case where the piezoelectric transducer surrounded by the ice (i.e. by placing the transducer in the water then decrease a temperature below freezing point), with the same water mass comparing to the previous case, when the water constantly changing its state to ice, the stiffness will also constantly increase. At the point where the ice film surrounding the transducer surface is thick enough, the effective stiffness of the system will increase to the point where the stiffness dominate the quantity of mass in the equation, resulting in increasing resonance frequency ($f_{ice} > f_{water} > f_{air}$).

Using these properties, we conducted experiments to verify whether the properties hold in other piezoelectric transducers. The piezoelectric transducer used in this experiment is model 7BB-20-6L0 from muRata as shown in Figure 5.1 and an experiment was set up as shown in Figure 5.2 below.
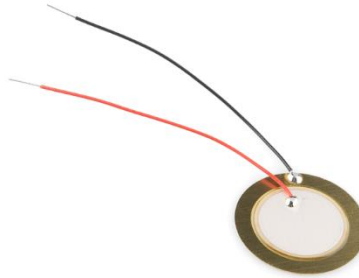

Figure 5.1 A piezoelectric transducer model 7BB-20-6L0 from muRata (Image reproduced from www.sparkfun.com)
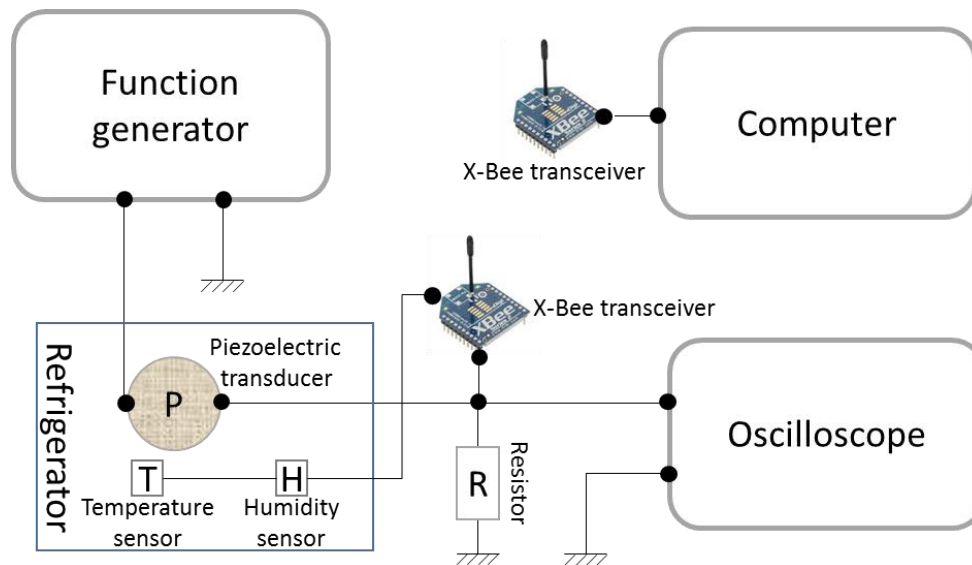

Figure 5.2 Circuit diagram used to test the piezoelectric transducer characteristics

As shown in Figure 5.2, a test environement has been set up by modifying a refridgerator in the way that we can monitor the ice formation in a container. Beside the piezoelectric transducer, we also implemented temperature sensors, and humidity sensor to monitor freezer and container surface's temperatures, and freezer's air humidity. The circuits required for operating the sensors were designed and implemented on the breadboard. The output of the sensors were fed to Xbee transmission module and transmitted wirelessly to the receiver module at the remote computer for data collection and analysis. The wireless data acquisition from the sensors and Xbee module was tested. Matlab is the main software used for data collection and analysis. Regarding to [6], the authors explained how they were able to distinguish the air, water, and ice

45

environment from the piezoelectric transducer outputs. The inputs of the piezoelectric transducer were fixed-amplitude (V_{p-p}) sinusoidal signals with different frequencies. The outputs will be the same-frequency sinusoidal signal but the phase and amplitude may be different from the original inputs based on the power used to excite the piezoelectric transducer itself (electrical power to vibration power). Again, we expected that the accumulation of water mass on the piezoelectric transducer surface would decrease the resonant frequency from its nominal value. In the case of ice accumulated on piezoelectric transducer surface, the effective stiffness of the piezoelectric transducer will increase proportionally to the ice thickness causing the resonant frequency to increase.

The piezoelectric transducer was placed into a container in the freezer in different conditions, water, and ice. We manually varied the frequency of input sinusoidal signal from 1 kHz to 100 kHz using a function generator and monitored the output of the piezoelectric transducer using an oscilloscope. The result confirmed that the output characteristic profiles of the piezoelectric transducer in different environment conditions, in this case, water, and ice, are different. However, since some output frequencies of sinusoidal signal range in the relatively high frequencies (10 kHz - 100 kHz), the speed of Xbee's analog to digital converter (ADC) would not be sufficient to digitize the signal. To solve this problem, we designed the circuit to convert sinusoidal output which is an alternating current (AC) to a direct current (DC) and monitored the changing in amplitude of the DC output. The plots of the outputs from the different frequency inputs in water and ice are shown in Figure 5.3 and 5.4 respectively.
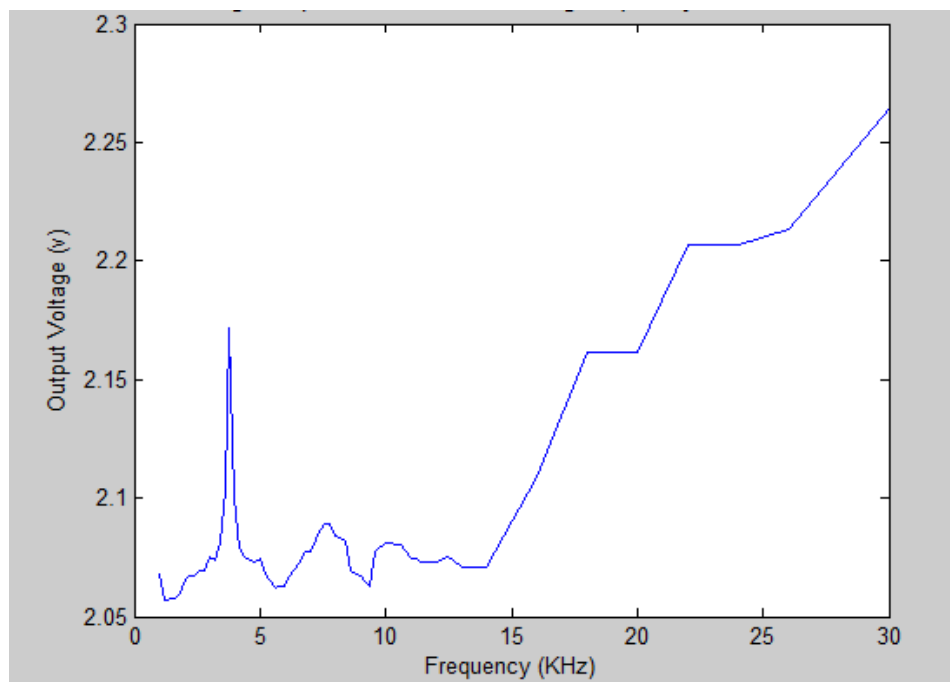

Figure 5.3 Characteristic profile of the output amplitude when placing the piezo in water
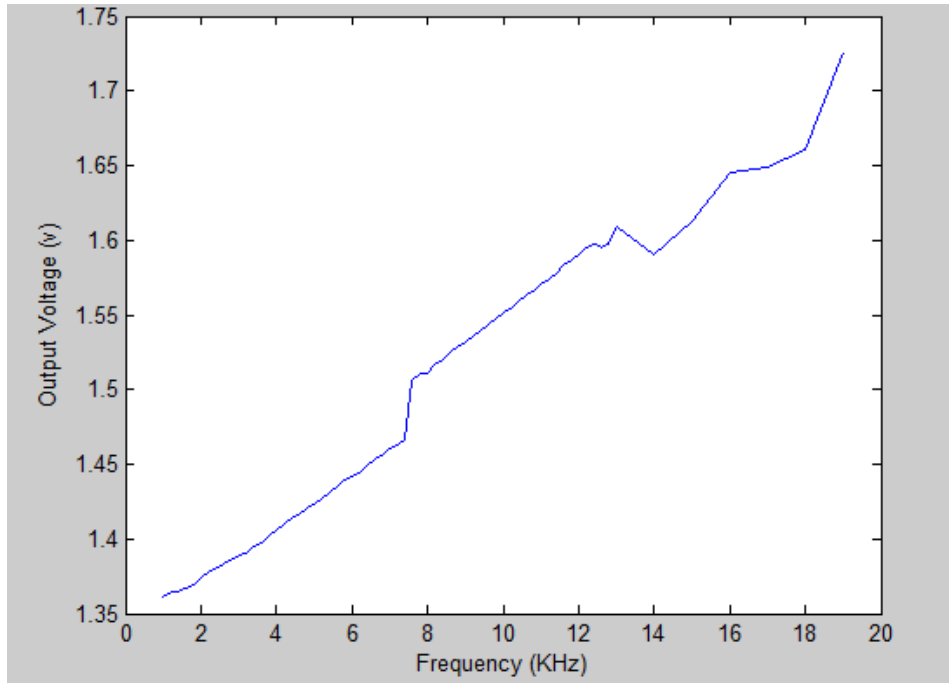
Figure 5.4 Characteristic profile of the output amplitude when placing the piezo in ice (thickness of 0.5 cm)

As seen from Figure 5.3, the maximum output response of the piezoelectric transducer occurs at the resonance frequency around 4 kHz of the sinusoidal input in the water environment. Then, the output amplitutes alternate in the frequency range of 4-10 kHz due to the harmonic responses. Once the input frequency was further increased after around 14 kHz, the output amplitudes increase rapidly and proportionally to the input frequency. Differently, as mentioned before, the accumulation of ice around the piezoelectric transducer would increase its resonance frequency. The result shown in Figure 5.4 supports the assumption very well. In stead of having a drastic peak as in water environment case, the output amplitude constantly increases proportionally with the input frequency right from the start freuquency at 1 kHz. This is because the resonance frequency of the piezoelectric transducer was shifted to higher frequency due to increasing of stiffness by the ice acuumulation around the piezoelectric transducer. Based on the differences in these two profiles, we should be able to further develop the system and statistical models to automatically distinquish the condition where the piezoelectric transducer was placed. Our current work focuses on conducting extensive tests to extract accurate classification criterias, and developing an electronic sensing system with integrated software for ice sensing.
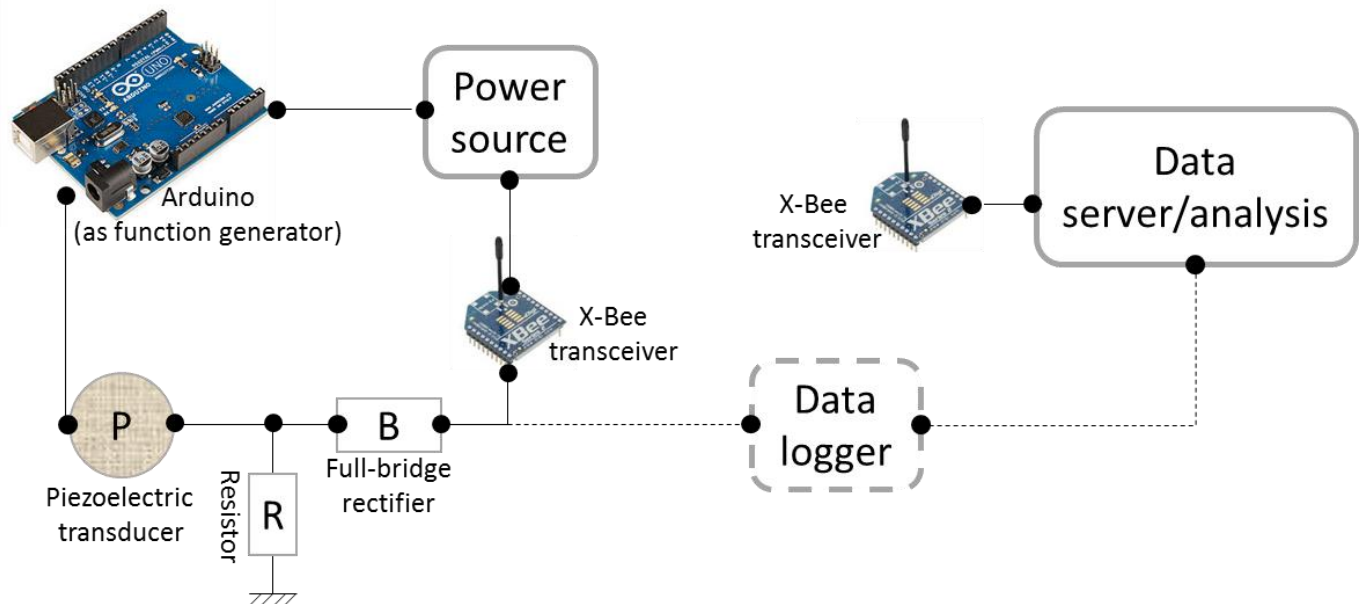
Figure 5.5 Overall system design of an automatic air, water, and ice detection system

5.2 System Design

Although we have proved that the concept of using a piezoelectric transducer to distinguish between water and ice states is valid. The next consideration is how to design the whole working system to be automatic, compact, and low-cost. It is impossible to have a person operating a full size function generator and oscilloscope in this particular application on the real site. With those constrains, we chose all electrical components which are low-cost yet reliable. All electrical components used in the design of an automatic air, water, and ice detection system are shown in Figure 5.5. To automate the process, we coded the Arduino to periodically generate square waves with frequencies ranging from 1 kHz to 100 kHz. The input frequencies will change discretely with the resolution of 1 kHz. The total time for each signal cycle (1 – 100 kHz) is approximately 22 seconds. These inputs were fed to a piezoelectric transducer which will be installed at the monitoring point. The original output from the piezoelectric transducer is relayed to a full-bridge rectifier to convert a square wave output (alternating current) to an equivalent RMS value (direct current) due to many reasons. First, to digitize the signal with a very high frequency (maximum at 100 kHz in this case), the sophisticate electrical component such as a microcontroller is needed. This will introduce more power consumption and less reliability of the system. Second, the change of the equivalent RMS value respecting to time which really is the focused signal used for the analysis is quite slow (maximum frequency less than 5 Hz). To save a transmission bandwidth and space needed for data storage, we choose to use a built-in digitizer either from Xbee transceiver or a data logger with a sampling frequency of 20 Hz. Then, these digitized data will be sent to a data storage and/or data analysis point either through wireless communication by Xbee transceiver or wire communication through a data logger. After the prototype of the system was built on a test board, we tested our concept by collecting the data from piezoelectric transducer in different states (air, water, and ice). The plots of each output pattern from each state are shown in Figure 6. From the Figure, it is clear that the signal patterns from the output of the piezoelectric transducer in different states are different

which suggests that we could use these output signals to classify the environment states. The analysis to classify a current state (air, water, or ice) may be done in real-time or by a periodic inquiry. Since all consideration about the hardware development was clarified, we will go through all data analysis and classification models development after this section. The data preprocessing process will be depicted in the next section.
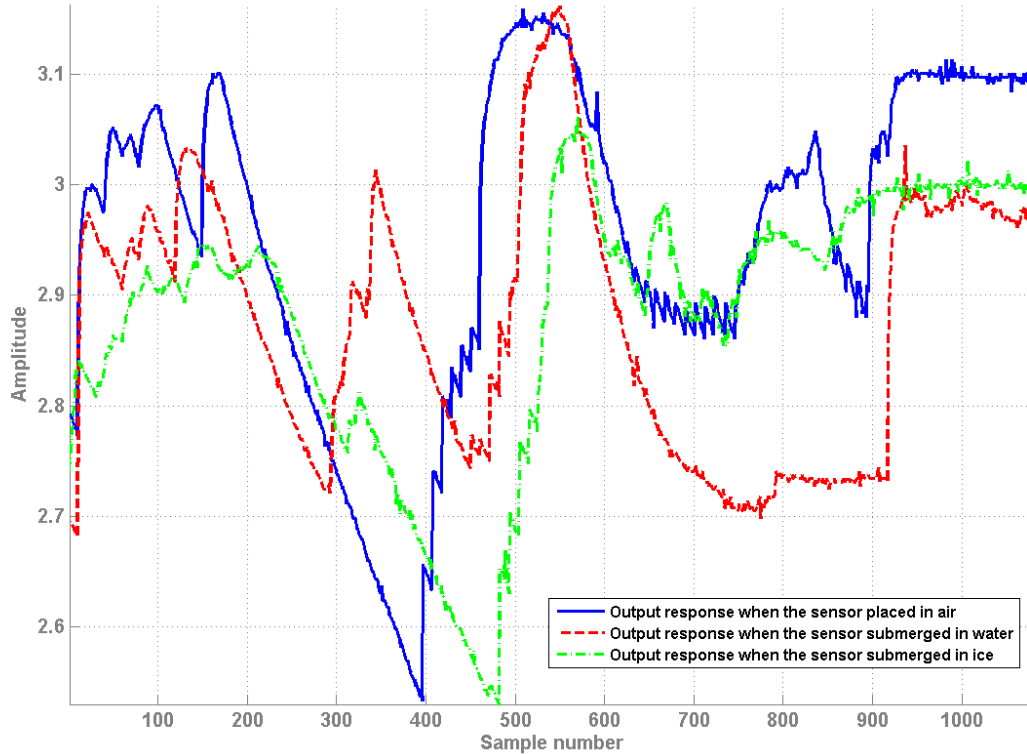

Figure 5.6 The piezoelectric transducer's output response profiles

5.3 Data Preprocessing

The transmitted data from the sensing point to a storage/analysis point has always been contaminated by interference signals. To capture only the wanted signal, the interference signals should be filtered out. The filtering process in this case takes two steps. First, interferences from a digitizing process of the Xbee transceiver cause some data samples to sharply drop its value to zero (i.e. abruptly changes from 1.5 V to 0 immediately in the next sample, then comes back to 1.5 V again in the next value). We designed the simple filtering process to check the rate of change of each output sample $(\frac{dy}{dt})$. The spurious data point with the rate of change from previous sample to the next value more than a specific threshold would be replaced by the value of the previous sample. The second step, from experiments, we found that the highest frequency characteristics of the output is around 1 Hz. Thus, the digital low-pass filter designed with an order of 300 and a cutoff frequency at 1 Hz is used for this filtering process. After these two steps, the data is normalized to range of (-1,1) with a zero mean. Finally, the data is clean and ready to be used in next section.

49

5.4 Feature Extraction

In this section, we will explain how the useful information from a piezoelectric transducer output (equivalent RMS value) is extracted and used for training classifier models before they could be used to differentiate environment states (air, water, or ice). We consider extracting features from two categories, time domain, and frequency domain.

In time domain, the assumption made is that each statistics of outputs from different input frequencies is different in each environment states (air, water, or ice). We calculate several statistics quantifications from each output segment that corresponding to each input frequency. For example, one input cycle accounts for 100 input frequency signal. Because the input frequency changes discretely with the resolution of 1 kHz in approximately 0.22 second for each level, if we can find the start and stop points of each input cycle, we can segment each output cycle to 100 segments corresponding to 100 input frequencies. (In our case, we also coded the Arduino to generate the signal that let us know the start and stop point of each input cycle.) The first output segment is the output from the square wave input with a frequency of 1 kHz and so on. We compute basic statistics namely, local average, local maxima, local minima, variance, and standard deviation of the data from each segment. Also, we fit the simple regression model and use its parameters namely, interception, and slope from the data from each segment as features. Next, the last feature is a frequency category of the input itself. Finally, there are 8 time domain features to be used in a modeling process.

For frequency domain feature extraction, we extract mel-scale frequency cepstral coefficient (MFCC) [7, 8] which is a standard feature set used in speech recognition application. In this case, we consider using a data length of 2 minutes or 2400 samples to extract MFCC features. The procedure is as followed. First, the data frame of 2400 samples is divided into segment by a sliding window technique for a suitable data length for a Discrete Fourier transform. In our case, we use a data length of 512 points with the overlapping of 40 points so that one data frame is segmented into 5 segments with the length of 512 points each. Next, we perform a Fast Fourier transform (FFT) to obtain the magnitude frequency response of each frame. Then, the magnitude frequency response is multiplied by a set of 50 triangular band-pass filters in order to obtain the log energy from each band-pass filter. Each filter has a pass-band bandwidth of 0.04 Hz and an overlap bandwidth with the previous filter for 0.02 Hz as shown in Figure 5.7 below.

Finally, we perform a discrete cosine transform (DCT) to the log energy of each band in order to transform the data in the frequency domain back into the time domain in the expression of a finite sequence of data points in terms of a sum of cosine functions oscillating at different frequencies. Finally, we have 50 frequency features to be used for an appropriate modeling technique which will be explained in the next section.
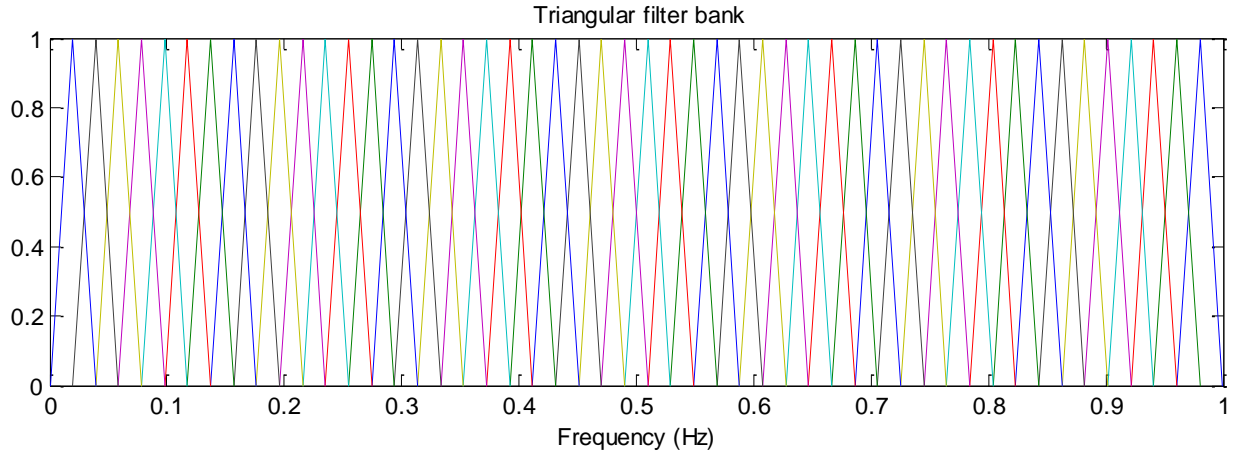
Figure 5.7 The triangular filter bank used for extracting frequency domain features

5.5 Classifier Development Methodologies

Before the features from both time and frequency domain could be used to train classification models, the class label must be assigned to each feature set or vector because we use the supervised learning classification methods. Practically, the data collected in different states (air, water, and ice) equally for eight hours were used in a training process. The features extract from each dataset will be accompany by the class number assigned to each state, Air: 1, Water: 2, and Ice: 3. From the preliminary analysis, the results suggest that two classifiers which are k-nearest neighbor and Gaussian mixture model work well in this application.

5.6 K-Nearest Neighbor

The k-nearest neighbor (kNN) is a nonparametric pattern classification method. It is a simple technique that the classification of a new feature set is performed by assigning them to the class which has the distance closest to them in the feature space. To be specific, the new feature set will be treated as a center of a circle sphere in N dimensional feature space (number of N depending on how many features used). The radius of the sphere will increase until there are k neighbors within the sphere. Finally, that new feature set will be classified to a class that has most frequent samples in the sphere. In our application, for this classifier, the time domain features tend to be good predictors in this case. However, using all 8 time domain features in this classification method will introduce a need of a very high computation power when classifies each new feature set since the distance of the new feature set will be calculated as a Euclidian distance in eight multidimensional feature space. To avoid the aforementioned problem, we perform a principle component analysis (PCA) to transform all features to three principle components (PC) and use these three PCs in a classification process. To represent the clustering behavior of the sensor outputs in different environments, the three dimensional plot from the most three important principle components is shown in Figure 5.8.
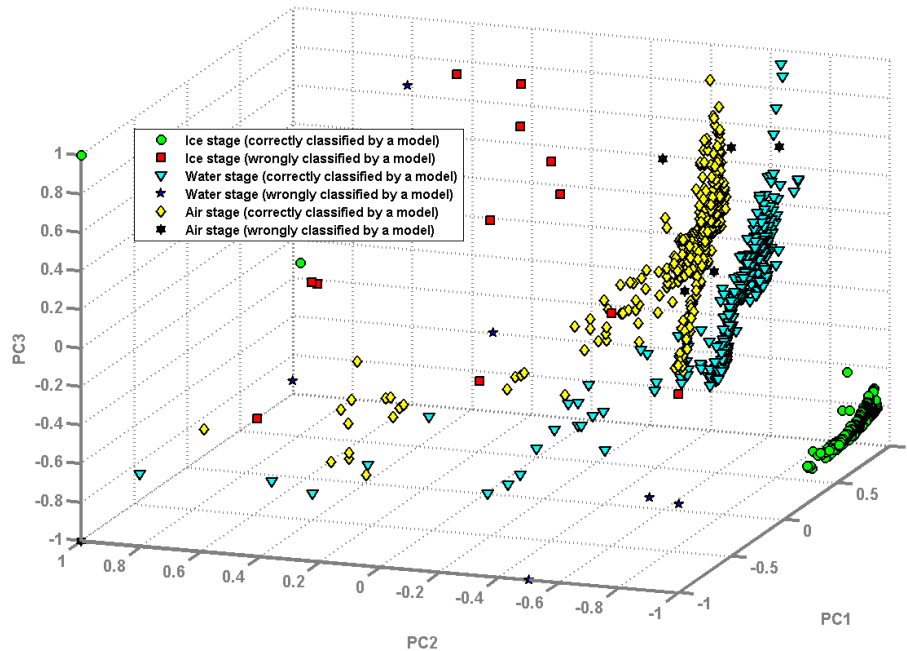
51

Figure 5.8 Three dimensional cluster plot of the sensor output's features from ice and water

In this plot, for an ice state, a green circle represents the point where the model could correctly classify the ice state and a red square represents the point where the model wrongly classify the ice state (predict as water or air state but the actual state is ice). Likewise, the cyan triangle in the plot represents the correctly classified water state and the blue star represents the point where the model classified the state as an ice but the actual state is air or water. To represent the air state, the yellow diamond is used where the model correctly classifies the air state from the observed output and the black hexagon shows where the model wrongly classifies the events as other states (water or ice). The cluster of each state clearly differentiates themselves from the others. Especially, the features from the ice state are clustered in a distance from the other two. Although, the data from water and air states seem to cluster closely to each other, there is a clear gap between the two clusters so that they could be discriminated properly. Again, since this plot is in 3 dimensions, it might not be enough to demonstrate the behaviors of the outputs in higher dimensions. The scatter points whose distances are so far from the cluster of each state in the left side of the plot are very good example in this case.

To implement this method, we split the data into two sets, training and validation, in the ratio of 80% and 20% respectively. The training dataset is used for searching for best parameters for the classification model. Then, these parameters are then used in the validation dataset to see the performance in the real world data. The result of the off-line classification performance from this method is shown below:

Training model: Accuracy rate: **97.74 %,** Sensitivity: **99.07%**, and Specificity: **96.99%.**
Validation model: Accuracy rate: **97.62 %**, Sensitivity: **98.55%**, and Specificity: **97.35%.**

5.7 Gaussian Mixture Model

Gaussian mixture model (GMM) is a parametric probability density function represented as a weighted sum of M Gaussian component densities as given by the equation [9]:

$$p(x|\lambda) = \sum_{i=1}^{M} w_i g(x|\mu_i, \Sigma_i)$$

Where x is a D-dimensional continuous data vector, w_i, i=1,…,M, are mixture weights, and $g(x|\mu_i, \Sigma_i)$, i=1,…,M, are Gaussian component densities. Each component density is a D-variate Gaussian function in a form of [9]:

$$g(x|\mu_i, \Sigma_i) = \frac{1}{(2\pi)^{D/2}|\Sigma_i|^{1/2}} \exp\{-\frac{1}{2}(x-\mu_i)^{\prime \Sigma_i^{-1}}(x-\mu_i)\}$$

Each unimodal Gaussian densities, $g(x|\mu_i, \Sigma_i)$, is parameterized by a mean D x 1 vector μ_i and a D x D covariance matrix Σ_i. Also, the mixture weights satisfy the constraint that $\sum_{i=1}^{M} w_i = 1$. Thus, the complete Gaussian mixture model is parameterized by mean vectors, covariance matrices, and mixture weights from all component densities. These parameters are denoted as: $\lambda = \{w_i, \mu_i, \Sigma_i\}, i = 1, …, M$. Intuitively, a GMM assumes that the distribution of the observed data is a combination of a mixture of several Gaussian distributions. Each individual distribution or mixture component may have different mean and variance. Some distributions may contribute more or less in the combination so that they are given the different weight in which their summation is equal to one. Thus, the final distribution could be obtained by multiplying each mixture component by its assigned weight then adding them together.

In this application, we assume that mean vectors, and covariance matrices are different for each feature set in each environment state (air, water, and ice). To classify a new feature set into each class, we estimate a maximum likelihood using the iterative expectation-maximization (EM) algorithm looking for the best match between the trained parameters of known classes and the new parameters of an unknown class. The EM algorithm iteratively refines the GMM parameters to monotonically increase the likelihood of the estimated model for the unknown class feature set. In each step of the algorithm, the unknown parameters are updated to their conditional maximum likelihood values. Finally, after some iterations, the parameter values converge to a local optimum. For test feature vectors, X={x₁,…,xT}, the log-likelihood of a trained model λ could be computed as [10]:

$$\log p(X|\lambda) = \sum_{t=1}^{T} \log p(x_t|\lambda)$$

To classify the test feature vector, the log-likelihood of each trained model derived from features of each environment state (air, water, and ice) and unknown class test feature

vector is computed then compared. The test feature vector will be classified into a class that gives the maximum log-likelihood computed previously. In our application, the result from experiments suggested that the optimum number of mixture component is ten. We have implemented this method to the data used in previous method and the performance of the GMM on the validation dataset is:

Accuracy on 'Air' status classification: **96.77 %**
Accuracy on 'Water' status classification: **98.59 %**
Accuracy on 'Ice' status classification: **97.87 %**

Each classification event for KNN is based on the data collected for 2 minutes, unlike in GMM method where the classification of the new feature set could be done in a fraction of a second. However, we found that the KNN modeling method uses very intensive computations (takes couple minutes) when making each classification (prediction). Since our aim in this application is to predict the environment state (air, water, or ice) in real-time, GMM is the better choice in this case.
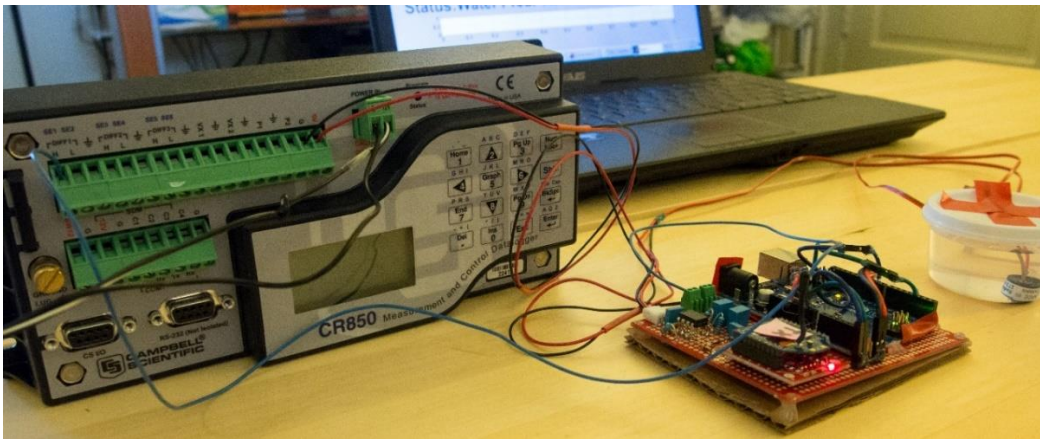

Figure 5.9 A hardware prototype set up with built-in Xbee socket and ability to connect to a data logger CR850 from Campbell Scientific
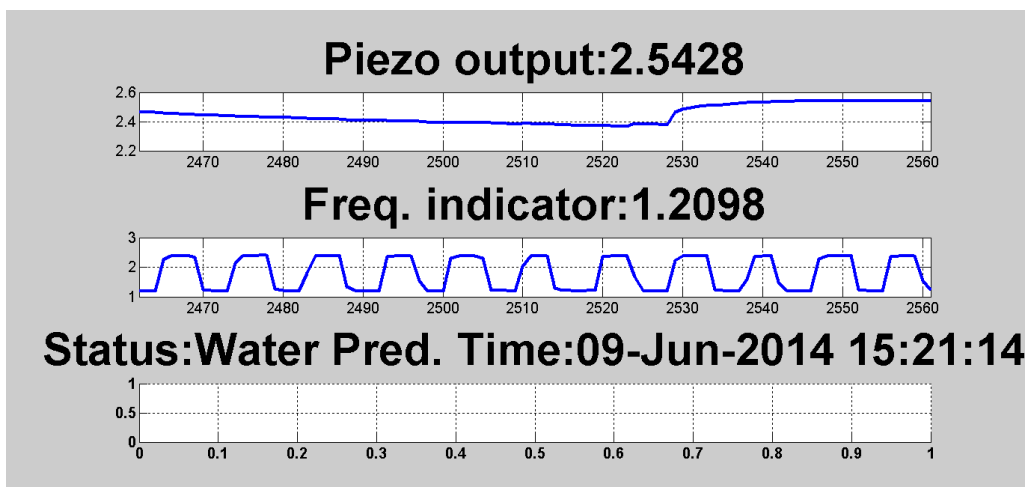

Figure 5.10 A screenshot of a real-time prediction software implemented in Matlab

54

5.8 Real-time Implementation Result

After the GMM classifier was developed, we combined the hardware prototype shown in Figure 5.9 and a real-time classification software (coded in Matlab) for testing in laboratory environment. The screenshot of a real-time prediction software is shown in Figure 5.10. The status screen shows the real-time output of the piezoelectric transducer with the prediction status that is updated every 2 minutes.

To make sure that the system could perform properly, we tested our system in the environment where the humidity and temperature were manipulated as close to the real "black ice" forming environment as possible. The scenario for forming the "black ice" is as followed: 1) the freezer is turned on to decrease the temperature constantly and will maintain the temperature at - 6 Celsius 2) the humidifier is also turned on in order to saturate the environment humidity (humidity close to 99% at all time). This scenario will surely create the invisible and very thin ice which is publicly called "black ice" on the surface of every object in the freezer. Comparing to previous experiments when we collected the data for training a model, we put the piezo sensor directly in a water-filled container in a freezer then let the ice form around the piezo sensor. The experiment setup is shown in Figure 5.11.
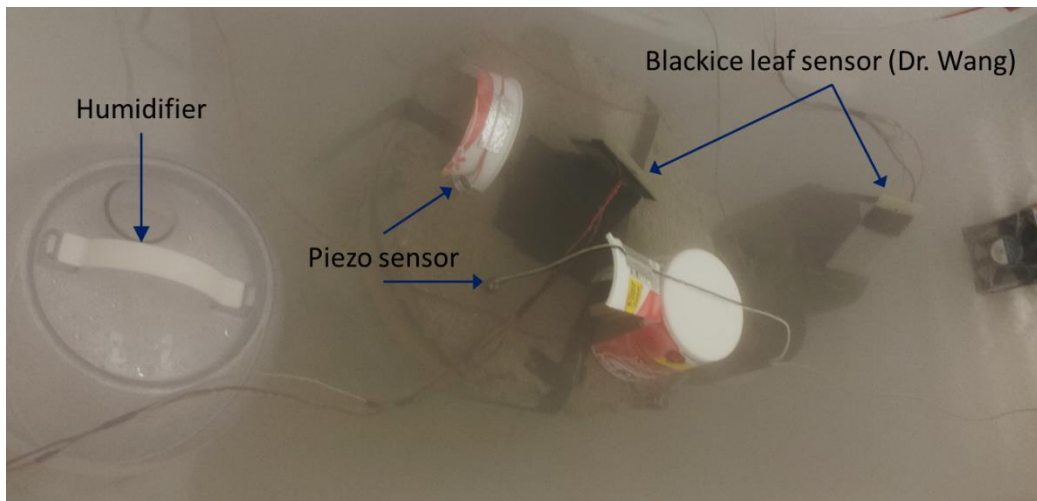

Figure 5.11 Environment and sensor set-up for the experiments

As seen from Figure 5.11, the piezoelectric transducer was placed as close to the concrete's surface as possible to eliminate the humidity and temperature differences. After all the hardware setup was in place, we close the freezer's door and let the ice form. The experiment was carried on for more than 8 hours to ensure that the thin layer of ice will surely form on every object's surface. With the results from previous experiments, the ice will be surely formed (noticeable) in the setup environment within 5 hours. The data collection and environment state prediction had been carried on simultaneously in real-time every 2 minute. Each prediction was performed based on the collected data length of the last 2 minutes. As shown in Figure 5.12, the first ice state prediction was reported at 14:32 which was around 4 hours from the start time. The environmental status at this time is: air temperature -0.247 Celsius, concrete temperature 2.324 Celsius, and humidity is 99.26%. Then, the prediction results were reported as alternating states between water

and ice states, with one false negative of air state in-between. Finally, the prediction results were steadily reported as ice states stating from 15:42 which was around 5 hours from the start time. The environmental status at this time is: air temperature -3.488 Celsius, concrete temperature -0.178 Celsius, and humidity is 99.26%. After that point, the prediction results were only ice states until the end of the experiment.
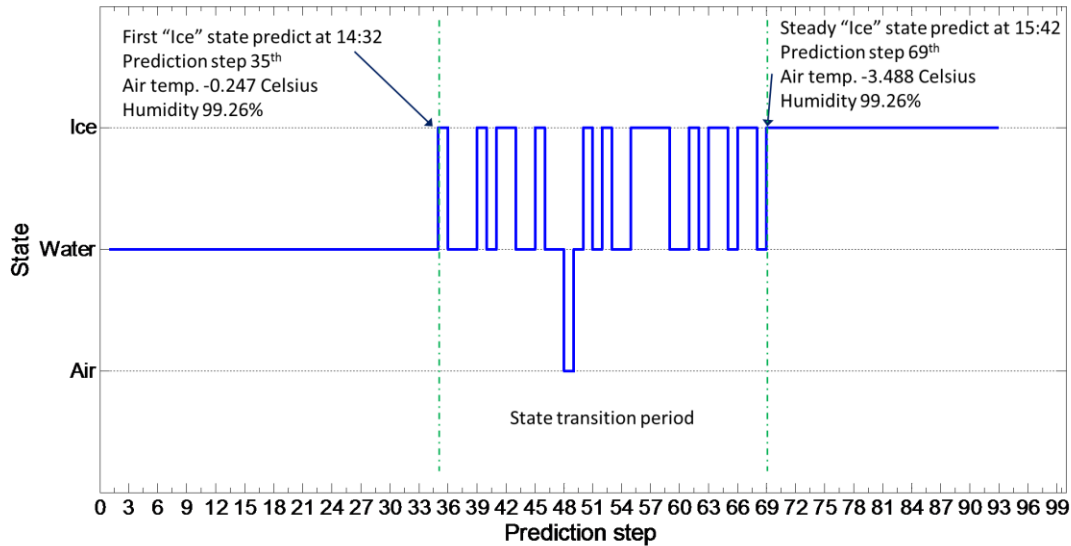

Figure 5.12 State prediction result from the piezo sensor and current model

5.9 Summary

The present work has demonstrated a novel approach for real-time detection of ice formation on roadways. The physical principle of the detection approach is based on discerning elastic stiffness and compliance changes associated with phase transformations. Key outcomes of the present work are summarized as follows:

1. Of-the-shelf piezoelectric sensors, microprocessors and low-power wireless modules were employed to develop a cost-effective sensing unit capable discerning the stiffness changes.
2. The sensor was tested using a laboratory test-bed available in the Sensor Networks and Complex Systems (COMMSENS) research lab at the Oklahoma State University. Signals from the wireless unit were processed at the base station computer for ice detection on different substrate materials pertinent to road highways.
3. Several alternative statistical classification approaches were investigated, and the experimental studies suggest that a Gaussian Mixture Model (GMM) would be best suited for real-time detection of ice formation with adequate sensitivity and specificity (all > 90% under tested conditions).

4. These investigations point to the viability of employing cost-effective roadside sensors for real-time detection of ice formation. Such an approach can drastically reduce the cost of installation and operation of a black-ice detection system.
5. Based on these results, we recommend additional laboratory studies involving phase transformations of water with different pH (and additives), on different substrates (concrete versus tar, with different surface topographies). Additionally, field tests on 2-3 bridges would be necessary to fully analyze the performance of the new approach.

References

1. *How Do Weather Events Impact Roads?* 2014 February 25, 2014 [cited 2014 October, 12]; Available from: http://www.ops.fhwa.dot.gov/weather/q1_roadimpact.htm.

2. Elman, E., *Novel cost-effective remote ice detection system allows extensive deployment.* Transport Research Arena Europe, 2008.

3. Innovative Dynamics, I. *IceSight.* [cited 2014 October, 12]; Available from: http://www.idiny.com/icesight.html.

4. Karki, J., *Signal Conditioning Piezoelectric Sensors.* App. Rept. on Mixed Signal Products (SLOA033A), Texas Instruments Incorporated, 2000.

5. Winterton, J.G., *Understanding √k/m - GE Measurement & Control.* ORBIT, 2006. **26**(2): p. 8.

6. Roy, S., et al., *Smart ice detection systems based on resonant piezoelectric transducers.* Sensors and Actuators A: Physical, 1998. **69**(3): p. 243-250.

7. Han, W., et al. *An efficient MFCC extraction method in speech recognition.* in *Circuits and Systems, 2006. ISCAS 2006. Proceedings. 2006 IEEE International Symposium on.* 2006. IEEE.

8. Muda, L., M. Begam, and I. Elamvazuthi, *Voice recognition algorithms using mel frequency cepstral coefficient (MFCC) and dynamic time warping (DTW) techniques.* arXiv preprint arXiv:1003.4083, 2010.

9. Reynolds, D., *Gaussian mixture models.* Encyclopedia of Biometrics, 2009: p. 659-663.

10. Reynolds, D.A., T.F. Quatieri, and R.B. Dunn, *Speaker verification using adapted Gaussian mixture models.* Digital signal processing, 2000. **10**(1): p. 19-41.

6. Development of the Remote Control Module

We developed a Road Closure Control Module. The Control Module will receive data from field sensors and send signals to turn on the warning lights of the roads and the bridges that are prone to forming black ice on the surface to prevent potential accidents and life losses.

Each wireless icing sensor and controller node consists of a radio depending on the distances from a nearby office. The radio will be used for communication between the datalogger at the sensing location. This will provide global wireless access to the sensor data via the Internet. A computer at Oklahoma State University (OSU) is configured as an FTP server as well as a Web server to receive, store, display, and manage the data.

The warning devices are designed to receive the control signal and other information from the DSS through their embedded radio modems. In the case that electricity is not available in the region, the warning devices will be powered by solar panels and batteries. The research team has built a sample warning device to demonstrate the functions of DSS.

6.1 The Integrated Black Ice Formation Sensing and Warning System

Figure 6.1 shows the overall architecture of the integrated black ice formation sensing and warning system, including a sensing unit, a warning unit, and a control unit.

1. Sensing unit:

   The sensing system consists of a black ice sensor and a thermocouple. The important merit of this design is to simplify the configuration with low cost. The thermocouple sensor was mounted on the surface of the selected black ice sensor. The outputs of both sensors were sent to a datalogger to retrieve the analog voltage signals.

2. Warning unit:

   A sharp LED warning light is controlled by the datalogger through the following conditions:

   - If the black ice sensor detects ice formation, the warning light will be turned on with the permission from the central server.

   - The warning light can also be turned on/off remotely by the commands from the central server, regardless of the sensor's output. This mode is only used in emergent situations or to test the status of the device.

3. Control unit:

   The control unit consists of a datalogger which is used to collect the data from sensors, control the warning light, and communicate with the central server through radios. The system program can be remotely uploaded to the datalogger from a server. The data collected by the datalogger can be remotely send to the server based on a preset schedule.

4. Power unit

The sensor and the datalogger is powered by a rechargeable battery pack inside the datalogger. A solar charging circuit can be added when needed.
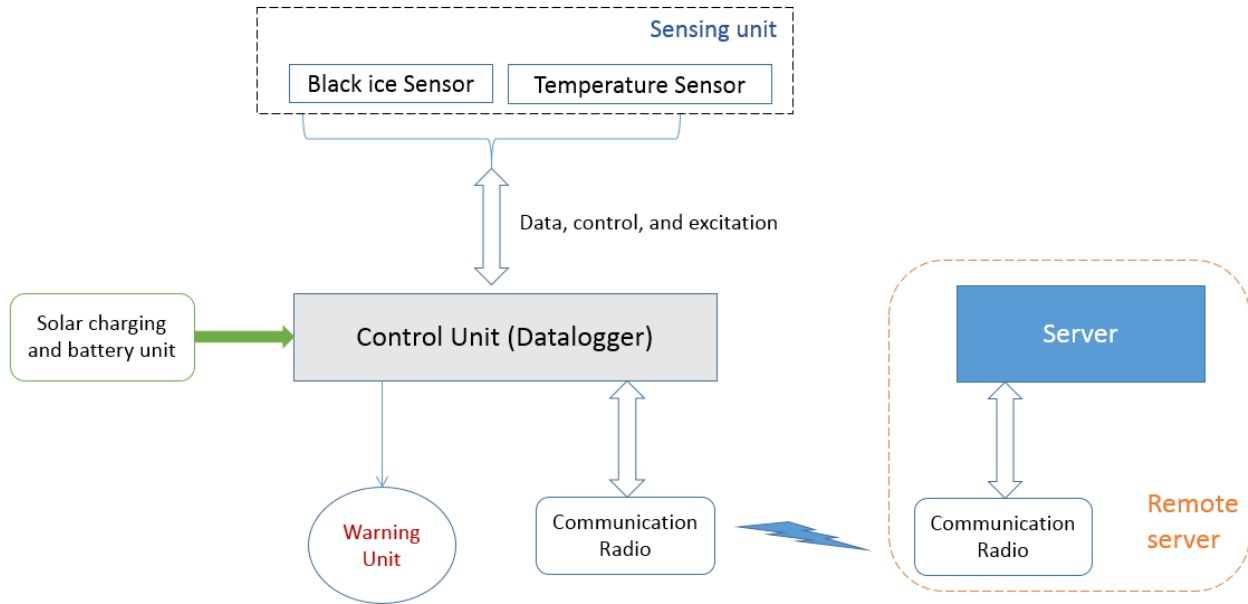

Figure 6.1 Overall architecture of the integrated black ice formation sensing and warning system

6.2 Network for Remote Control Module

Figure 6.2 shows the current network structure between a remote station and a base station (central server) through 2.4GHz radio communications. Multiple remote stations could be added to the network with simple configurations of a pre-assigned address. The radio used in the system is a 2.4 spread spectrum radio from Campbell scientific Inc. It supports pointed-to-point and point-to-multipoint communication. With the 0 dBd, ½-wave whip antenna, the radio can transmit data reliably within a short distance (<50m). In the deployment of the development system, a directional high-gain antenna can be used for longer distance transmission.

The server can send signals to the datalogger(s) and collect data from every datalogger. In addition, under certain situation, the server could send command to turn on/off the warning light remotely.

A water-proof enclosure is selected to deploy the remote stations in outdoor environment. The integrated black-ice warning system is housed inside the enclosure and can be connected with selected solar panel for charging when needed (Figure 6.3).
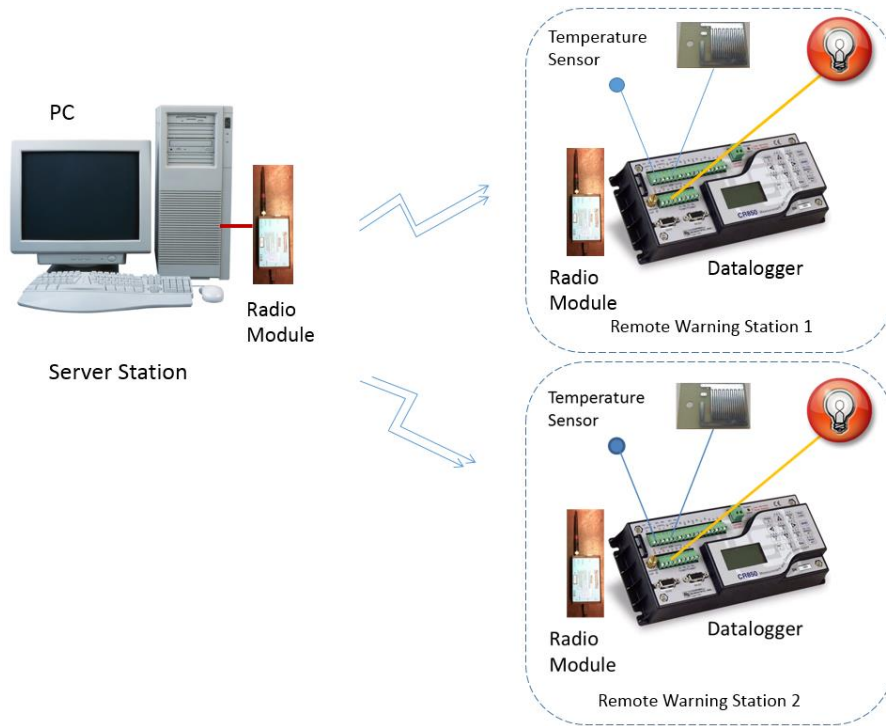
Figure 6.2 Network architecture of the develop black-ice warning system
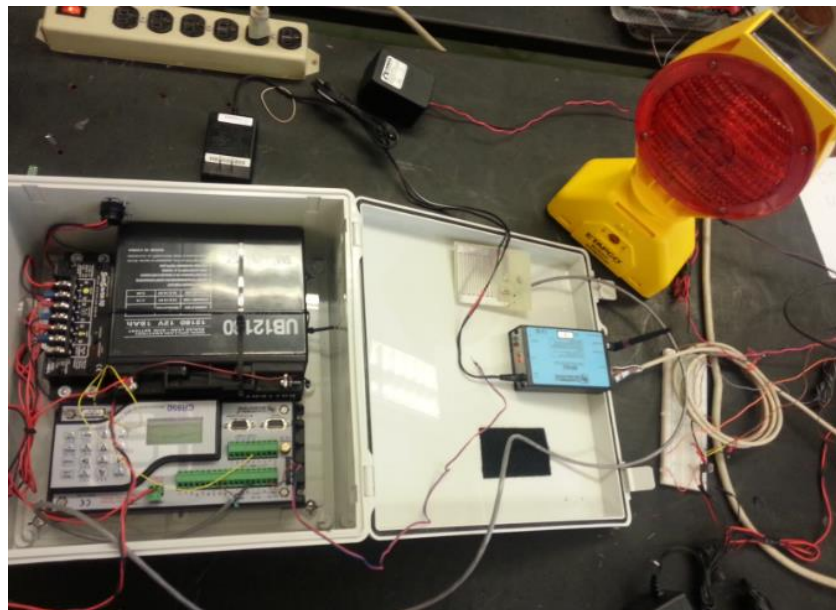

Figure 6.3 Water-proof enclosure for the remote station

6.3 Road Closure Control Module at the Central Server

A computer connected with a radio module is configured as a central server to receive, store, display, and manage the data. If an alarm signal needs to be issued, the central server can send a command to the on-site sensor package through the network to signal the warning.

The interface of the Road Closure Control Module is shown in Figure 6.4. There are two control modes: manual control and automatic control.
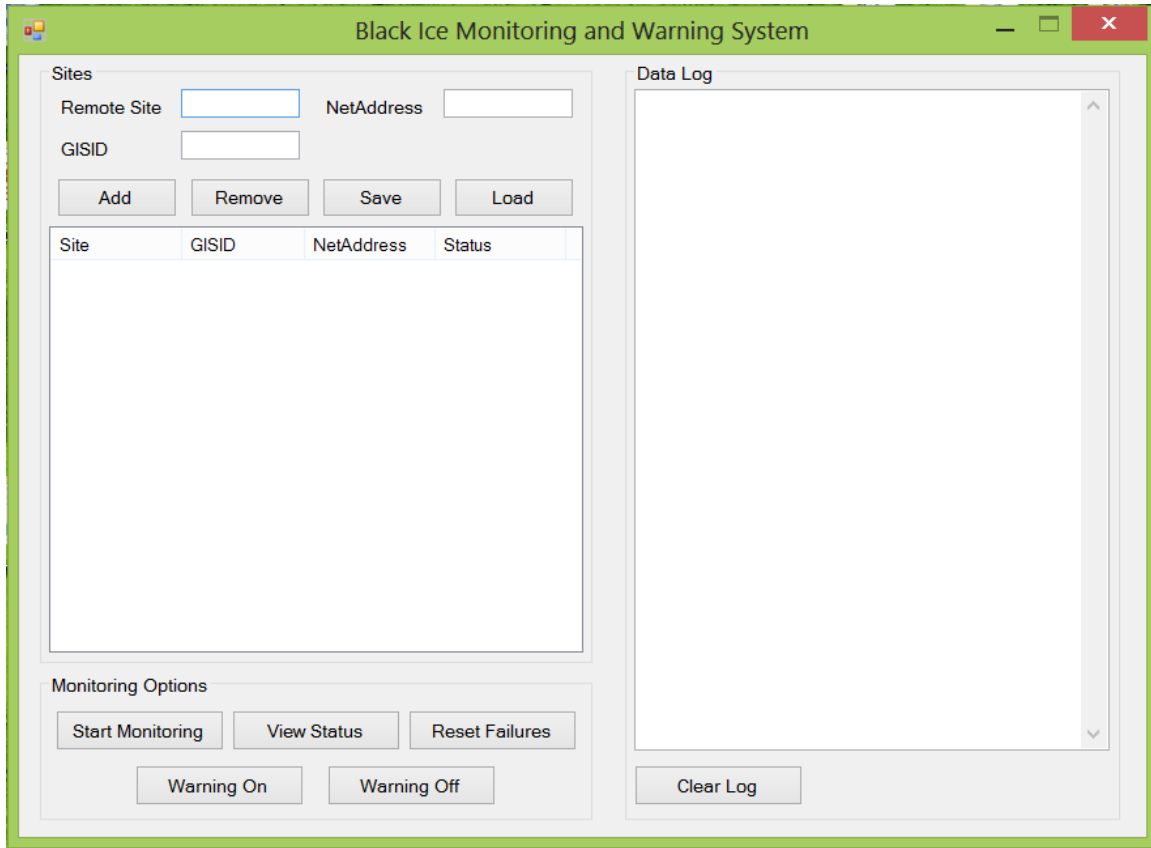

Figure 6.4 Interface of the Road Closure Control Module

Automatic control: The automatic control function will be turned on by clicking the "Start Monitoring" button. By calling the GIS Spatial Database, the Road Closure Control Module can identify the road segments where black ice is predicted. In the site window, the color of the sites with black ice warnings will change to orange. Then the server will communicate with the dataloggers on those road segments. Meanwhile, the Data Log window will show to which sites the server has sent the warning and if the lights have been turned on.

Then, the data from the ice sensors and the temperature sensors on those road segments will be collected. Once both of the ice formation and temperature thresholds

are satisfied, the Road Closure Control Module will turn on the warning lights automatically. If the black ice warnings for the road segments are cleared, the Road Closure Control Module will turn off the warning lights.

By clicking the "Stop Monitor" button, the system will stop monitoring the GIS Spatial Database and the remote sites, and all the warning lights will be turned off as well.

Manual control: As shown in Figure 6.5, by selecting the sites from the site window and then clicking the "View Status" button, the system will start to collect the data from the checked sites. The data collected will be shown in the Data Log window, and the warning status will be displayed in the site window. After clicking the "View Status" button, if the light of a selected site is on, the status in the site window will become "Alarm On". The system will also output the address of the sites where the lights are on and depict those sites to the GIS map.
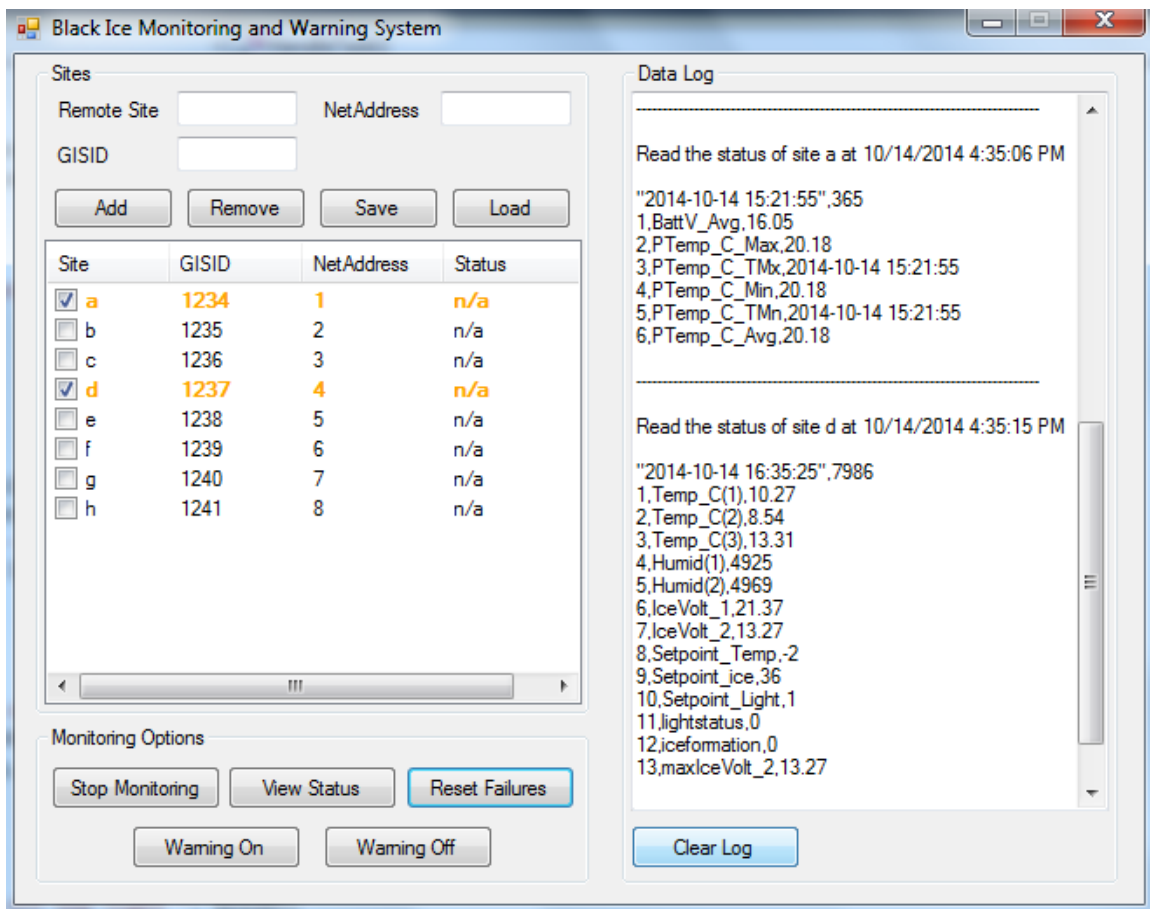

Figure 6.5 View the status of site a and d by clicking "View Status" button

If an officer wants to turn on/off the light of a remote site based on his decision, it can easily be done by clicking the "Warning On" and "Warning Off" buttons, as seen in Figure 6.6. Meanwhile, the "Warning On" button can also be used to test if a remote light works appropriately.
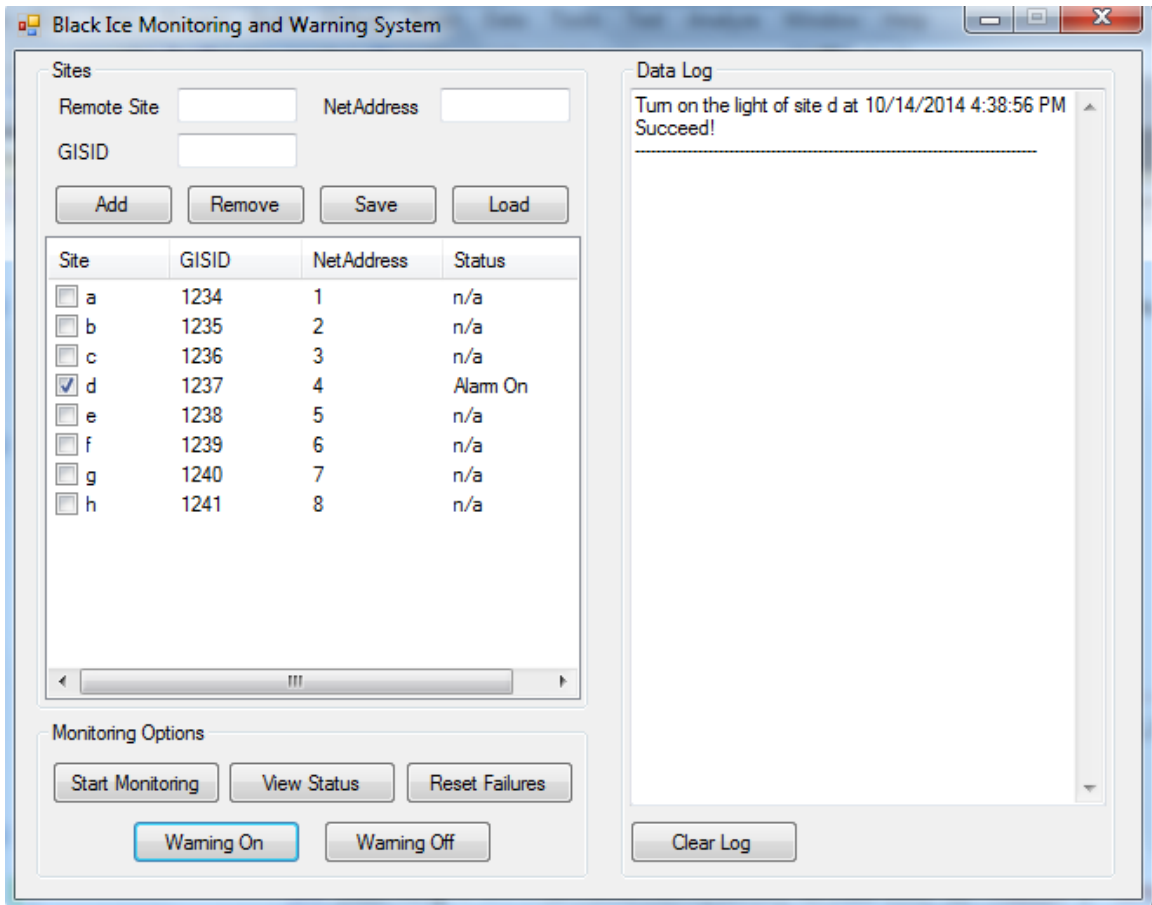
Figure 6.6 Turn on the light of site d by clicking "Warning On" button

.